NASA / TM-2000-209846
ARL-TR-2205

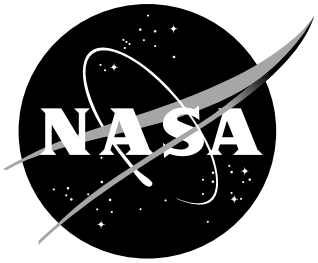

Active Structural Acoustic Control of Interior Noise on a Raytheon 1900D

Dan Palumbo and Ran Cabell
Langley Research Center, Hampton, Virginia

John Cline
U.S. Army Research Laboratory
Vehicle Technology Directorate
Langley Research Center, Hampton, Virginia

Brenda Sullivan
Langley Research Center, Hampton, Virginia

March 2000

The NASA STI Program Office ... in Profile

Since its founding, NASA has been dedicated to the advancement of aeronautics and space science. The NASA Scientific and Technical Information (STI) Program Office plays a key part in helping NASA maintain this important role.

The NASA STI Program Office is operated by Langley Research Center, the lead center for NASA's scientific and technical information. The NASA STI Program Office provides access to the NASA STI Database, the largest collection of aeronautical and space science STI in the world. The Program Office is also NASA's institutional mechanism for disseminating the results of its research and development activities. These results are published by NASA in the NASA STI Report Series, which includes the following report types:

- TECHNICAL PUBLICATION. Reports of completed research or a major significant phase of research that present the results of NASA programs and include extensive data or theoretical analysis. Includes compilations of significant scientific and technical data and information deemed to be of continuing reference value. NASA counterpart of peer-reviewed formal professional papers, but having less stringent limitations on manuscript length and extent of graphic presentations.

- TECHNICAL MEMORANDUM. Scientific and technical findings that are preliminary or of specialized interest, e.g., quick release reports, working papers, and bibliographies that contain minimal annotation. Does not contain extensive analysis.

- CONTRACTOR REPORT. Scientific and technical findings by NASA-sponsored contractors and grantees.

- CONFERENCE PUBLICATION. Collected papers from scientific and technical conferences, symposia, seminars, or other meetings sponsored or co-sponsored by NASA.

- SPECIAL PUBLICATION. Scientific, technical, or historical information from NASA programs, projects, and missions, often concerned with subjects having substantial public interest.

- TECHNICAL TRANSLATION. English-language translations of foreign scientific and technical material pertinent to NASA's mission.

Specialized services that complement the STI Program Office's diverse offerings include creating custom thesauri, building customized databases, organizing and publishing research results ... even providing videos.

For more information about the NASA STI Program Office, see the following:

- Access the NASA STI Program Home Page at ***http://www.sti.nasa.gov***

- E-mail your question via the Internet to help@sti.nasa.gov

- Fax your question to the NASA STI Help Desk at (301) 621-0134

- Phone the NASA STI Help Desk at (301) 621-0390

- Write to:
  NASA STI Help Desk
  NASA Center for AeroSpace Information
  7121 Standard Drive
  Hanover, MD 21076-1320

NASA/TM-2000-209846
ARL-TR-2205

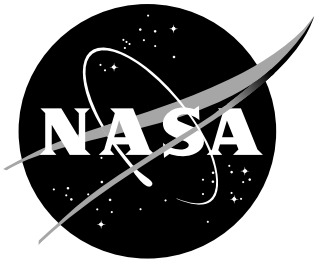

Active Structural Acoustic Control of Interior Noise on a Raytheon 1900D

Dan Palumbo and Ran Cabell
Langley Research Center, Hampton, Virginia

John Cline
U.S. Army Research Laboratory
Vehicle Technology Directorate
Langley Research Center, Hampton, Virginia

Brenda Sullivan
Langley Research Center, Hampton, Virginia

National Aeronautics and
Space Administration

Langley Research Center
Hampton, Virginia 23681-2199

March 2000

The use of trademarks or names of manufacturers in the report is for accurate reporting and does not constitute an official endorsement, either expressed or implied, of such products or manufacturers by the National Aeronautics and Space Administration or the U.S. Army.

Available from:

NASA Center for AeroSpace Information (CASI)
7121 Standard Drive
Hanover, MD 21076-1320
(301) 621-0390

National Technical Information Service (NTIS)
5285 Port Royal Road
Springfield, VA 22161-2171
(703) 605-6000

Abstract

An active structural acoustic control system has been demonstrated on a Raytheon Aircraft Company 1900D turboprop airliner. Both single frequency and multi-frequency control of the blade passage frequency and its harmonics was accomplished. The control algorithm was a variant of the popular filtered-x LMS implemented in the principal component domain. The control system consisted of 21 inertial actuators and 32 microphones. The actuators were mounted to the aircraft's ring frames. The microphones were distributed uniformly throughout the interior at head height, both seated and standing. Actuator locations were selected using a combinatorial search optimization algorithm. The control system achieved a 14 dB noise reduction of the blade passage frequency during single frequency tests. Multi-frequency control of the first 1^{st}, 2^{nd} and 3^{rd} harmonics resulted in 10.2 dB, 3.3 dB and 1.6 dB noise reductions respectively. These results fall short of the predictions which were produced by the optimization algorithm (13.5 dB, 8.6 dB and 6.3 dB). The optimization was based on actuator transfer functions taken on the ground and it is postulated that cabin pressurization at flight altitude was a factor in this discrepancy.

Introduction

An active structural acoustic control (ASAC) system has been demonstrated on a Raytheon Aircraft Company 1900D turboprop airliner. The ASAC approach has been in development for several years [1,2,3,4,5,6] and has been demonstrated previously in at least one other test [34]. ASAC differs from the more common active noise control (ANC) [35,36,37,7,8,9] approach in actuation method; ANC using loudspeakers versus ASAC's structural actuators. For this flight test, inertial actuators were employed which were mounted directly to the 1900D frame. The ASAC approach has been pursued with the expectation that a mature design will be more cost effective than an ANC system of comparable performance. Improvements are expected in installation costs, channel count and channel power requirements.

Two new technologies were tested in the ASAC design. The filtered-x LMS [10,11,12] controller was implemented in the principal component domain [13]. This uncoupled architecture makes possible processing efficiencies and controller stability beyond that of conventional controllers. Also, the actuator locations were optimized using combinatorial search techniques that were directed by predictions of noise reduction and control force [14,15]. Proper positioning of ASAC actuators has been shown to be critical in achieving good noise control [5,6,16].

The flight test objectives were to demonstrate stable noise control of the first 3 harmonics of the blade passage frequency, bpf, verifying controller performance and validating the optimization predictions. Both single frequency and multi-frequency control were accomplished.

The following sections present a description of the principal component controller, the optimization procedure, the 1990D and the test configuration. Results are presented and discussed, and concluding remarks offered.

Principal Component Controller

A principal component least mean squares (PC-LMS) algorithm was used as the adaptive control algorithm for these flight tests. This algorithm is a transform domain version of the multi-channel filtered-x LMS algorithm [7,12], and is described in detail elsewhere [13]. In PC-LMS the controller parameters (filter weights) are adapted in a transformed coordinate system that decouples the feedforward control system at a single frequency. Each control channel is independent of every other channel. In contrast, the filter weights for the filtered-x algorithm are adapted in a coordinate system defined by the control actuators, which are not usually independent of one another and can often show high degrees of inter-channel coupling when many actuators are used. By decoupling the control channels, convergence rates and control effort penalties can be set for each channel independently.

A block diagram of a feedforward controller based on the multiple error LMS algorithm is shown in Figure 1. The response of the error sensors is given by the (mx1) vector **e**, and at a frequency ω as described by the expression

$$\mathbf{e}(\omega) = \mathbf{H}(\omega)\mathbf{w}(\omega) + \mathbf{d}(\omega) \qquad (1)$$

The (rx1) vector **w** contains the control inputs to the actuators, and the (mxr) matrix **H** contains transfer functions from the output of each actuator to the input of each error sensor at the frequency ω. The (mx1) vector **d** holds the error sensor responses to the primary noise field, and is called the primary response. The matrix $\hat{\mathbf{H}}(z)$ is an estimate of the error path transfer function matrix **H**(z), and filters the incoming reference signal as part of the multiple error LMS algorithm [12].

Each term in (1) depends on frequency ω, and this dependence is implicitly understood in subsequent equations. The frequency domain representation in (1) describes the controller operating at steady state, with no transients, and should not be used to analyze the effect of delays in the error path transfer functions on the controller [7,11].

The PC-LMS algorithm is obtained by substituting the singular value decomposition (SVD) of **H** into (1). The SVD of **H** is written

$$\mathbf{H} = \mathbf{U}\mathbf{S}\mathbf{V}^{H} \qquad (2)$$

where $()^{H}$ denotes the complex conjugate transpose. The (mxm) matrix **U** and (rxr) matrix **V** contain the eigenvectors of $\mathbf{H}\mathbf{H}^{H}$ and $\mathbf{H}^{H}\mathbf{H}$, respectively. The (mxr) matrix **S** contains the square roots of the eigenvalues, or singular values, of $\mathbf{H}^{H}\mathbf{H}$. The singular values are decreasing, such that $s_1 > s_2 > ... > s_r$, where s_i is the i^{th} singular value.

Substituting the SVD of **H** into (1) yields

$$\mathbf{e} = \mathbf{U}\mathbf{S}\mathbf{V}^H\mathbf{w} + \mathbf{d} \qquad (3)$$

$$\mathbf{U}^H\mathbf{e} = \mathbf{S}\mathbf{V}^H\mathbf{w} + \mathbf{U}^H\mathbf{d} \qquad (4)$$

$$\boldsymbol{\zeta}\mathbf{e} = \mathbf{S}\nu + \mathbf{p} \qquad (5)$$

The columns of **U** and **V** are used to transform sensor inputs and actuator responses, respectively, into the principal coordinates, or principal components (PCs), of the control system [13,17]. The vector $\boldsymbol{\zeta} = \mathbf{U}^H\mathbf{e}$ denotes the mapping of the sensor responses onto the PCs, and $\boldsymbol{\nu} = \mathbf{V}^H\mathbf{w}$ denotes the mapping of the actuator inputs onto the PCs. The vector $\mathbf{p} = \mathbf{U}^H\mathbf{d}$ is the mapping of the primary field onto the PCs.

Expanding the transformed system given by (5) term by term produces

$$\zeta_i = \begin{cases} s_i\nu_i + p_i & \text{for i} = 1,\cdots,\text{r} \\ p_i & \text{for i} = \text{r}+1,\cdots,\text{m} \end{cases} \qquad (6)$$

assuming there are more error sensors than control actuators. Each PC error term, ζ_i, thus depends only on the corresponding PC control input, ν_i, and the mapping of the primary response onto the i^{th} PC. The last $(r+1)$ through m PCs are not controllable, and constitute the residual field after control is applied.

Figure 2 contains a schematic of a feedforward control system implemented using the PC-LMS algorithm. The filter weights, **ν**, are adapted in terms of the PCs of the controller, and then transformed using **V** into actuator coordinates. The sensor responses are likewise transformed into PC coordinates using $\mathbf{U}^H$ and used in the recursive updates of the filter weights in PC coordinates.

A recursive update for the PC control inputs, ν_i, is easily derived from the weight update expression used in the multiple error LMS algorithm. The adaptive algorithm for the i^{th} PC weight, ν_i, is written [13]

$$\nu_i(n+1) = \nu_i(n) - \mu_i s_i \zeta_i(n) \qquad (7)$$

Combining the step size, μ_i, and singular value, s_i, into a single value yields a generalized update,

$$\nu_i(n+1) = \nu_i(n) - \alpha_i \zeta_i(n) \qquad (8)$$

where α_i is the step size parameter for the i^{th} principal component.

It is often necessary to constrain the control outputs so they do not exceed physical limitations of the

control actuators. This can be done in two ways with the PC-LMS algorithm: (1) disable the high order PC channels associated with high control forces [13,17,18], by zeroing the step sizes, α_i , or (2) apply a control effort penalty to limit the maximum value of each PC control input. The update recursion with control effort penalty, β, is written

$$v_i(n+1) = \left(1 - \frac{\mu_i}{s_i}\beta_i\right) v_i(n) - \alpha_i \zeta_i(n) \qquad \textbf{(9)}$$

The noise reduction potential of candidate control systems is calculated during actuator location optimization. For a feedforward control system, predictions of noise reduction and control effort require knowledge of the transfer function matrix, **H**, the primary response, **d**, and an estimate of the coherence between the reference and the primary response, γ_i^2 . The portion of the primary response at the i^{th} microphone that is coherent with the reference signal, and therefore controllable, is given by

$$d_i^{coh} = d_i \gamma_i \qquad \textbf{(10)}$$

In (10), γ_i^2 is the coherence between the reference and the response of the i^{th} microphone. Applying the PC transformation to the coherent portion of the primary response, d_i^{coh} , produces a vector of coherence PC responses, denoted p_i^{coh} . The predicted value of the control input to the i^{th} PC is given by [13,17]

$$v_i^{pred} = \frac{-s_i p_i^{coh}}{s_i^2 + \beta_i} \qquad \textbf{(11)}$$

The predicted control inputs in terms of actuator coordinates can be computed from the PC control inputs, $\mathbf{v}^{pred}$, as

$$\mathbf{w}^{pred} = \mathbf{V} v^{pred} \qquad \textbf{(12)}$$

The predicted control inputs, $\mathbf{w}^{pred}$, can be used with the coherent primary response, $\mathbf{d}_i^{coh}$, in (1) to estimate noise reduction. An alternative approach to estimating noise reduction is used during optimization of actuator locations. This approach is explained in the following sections.

Actuator Location Optimization

An active noise control system's performance can be measured by the degree of noise reduction achieved and is, thus, dependent on the placement of both the actuators and sensors. If sensor location is optimized for greatest noise reduction, inevitably the optimum sensor topology would be one in which the sensors are not uniformly distributed throughout the cabin interior. Because the ultimate metric of noise control in aircraft interiors is the comfort of the passengers seated throughout the cabin, it was decided that a non-optimized, uniform sensor array was the best approach. Using a uniform array also provides a measure of the global control obtained by the system. Thus it is necessary to optimize actuator locations. Several different methods have been applied to this problem [16,19,20,21,22,23,24,25,26]. A combinatorial

search method was chosen based on its simplicity and past success in its application to the actuator optimization problem [15,27].

Combinatorial Search

A combinatorial search systematically examines all subsets of a large set of candidates, retaining those that best meet some goal or performance criterion. For the purpose of optimizing actuator locations for maximum noise reduction, a database of actuator responses at each candidate location must be constructed and a procedure for predicting the noise reduction for any subset of actuators must be established.

There are pitfalls to implementing a combinatorial search which can be avoided through proper choice of technique. One problem is the size of the search space that must be traversed to locate the optimal subset. As an example, consider an exhaustive search for a 25 element actuator array given 100 possible locations for the actuators on the aircraft. The number of trials that must be done is given by the *combination* operator:

$$\left(\frac{N_a!}{(N_a - N_c)! * N_c!} \right) \qquad \textbf{(13)}$$

where N_a is the number of possible locations (100) and N_c is then size of the actuator array (25). This yields over 2.4×10^{23} possible combinations. An alternative to exhaustive search is a goal directed search in which the optimal set is continually refined in the direction of ever increasing noise reduction through selective substitution. This method has the drawback that it might settle into a local minimum that is far removed from the global optimum. Attempts to climb out of the local minimum are complicated by the tendency for the search to eventually slide back into the same minimum, thus introducing cycling.

Tabu Search

The tabu search method avoids the pitfalls mentioned above and has been used successfully to construct optimum arrays of actuators and sensors [15,27]. Tabu search maintains a list of past configurations (the tabu list) which are checked regularly to prevent the cycling problem. Table I contains a list of components that will be used in the following description of the tabu search algorithm.

1) Select an arbitrary state as **Current State**.
2) Loop for N_i Iterations
    a) Put **Current State** on **Tabu List**
    b) If **Cost Function** is minimum, save **Current State**.
    c) Evaluate **Cost Function** of all **States** in **Neighborhood**.
    d) **Move** to new **Current State** not on **Tabu List** which either
        i) Reduces the **Cost Function** the most, **OR**,
        ii) Increases the **Cost Function** the least

Using this algorithm, the search will climb out of a local minimum and not cycle back. A drawback of the tabu search algorithm is that it is not guaranteed to find the global minimum for any fixed number of iterations less than those required for an exhaustive search. However, experience has shown that, for the actuator location problem, good solutions are found quickly. Taking again the example of finding the

best 25 actuator locations out of a possible 100, each iteration of the tabu search algorithm will require 75 evaluations of the cost function (the size of the **Neighborhood**). The tabu search algorithm will typically find a good solution in less than 100 iterations (a total number of 7,500 evaluations or trials).

The effectiveness of the tabu search algorithm hinges on the accuracy of the cost function (predicted noise reduction) and the coverage of the candidate pool. Absolute accuracy is not necessary for optimization. However, to make tradeoffs on the number of actuators needed to meet a specific noise reduction goal, a reasonably accurate prediction is needed. Acquiring the data necessary to construct the candidate pool is also challenging because it requires obtaining a representative sample of the actuator responses at all the possible locations. The next two sections review the approaches taken in these two areas.

Noise Reduction Prediction

An expression for noise reduction can be derived for the control system as shown in Figure 1 using the equation for the response of the error sensors given by (1) and repeated here for the single frequency case.

$$\mathbf{e}_{\min} = \mathbf{H}\mathbf{w}_{opt} + \mathbf{d} \qquad \textbf{(14)}$$

Maximum noise reduction is obtained when the error response, $\mathbf{e}_{\min}$, is minimized. The LMS algorithm will find the optimum control force, $\mathbf{w}_{opt}$, by minimizing a cost function given by the squared norm of the error response.

$$J = \mathbf{e}^{\mathrm{H}}\mathbf{e} \qquad \textbf{(15)}$$

An analytical solution exists for (15) [7,11,12] and is given by

$$\mathbf{w}_{opt} = -\left(\mathbf{H}^{\mathrm{H}}\mathbf{H}\right)^{-1}\mathbf{H}^{\mathrm{H}}\mathbf{d} \qquad \textbf{(16)}$$

The predicted noise reduction in dB then becomes

$$\Delta_{dB} = 10\log_{10}\left(\frac{\mathbf{e}_{\min}^{H}\mathbf{e}_{\min}}{\mathbf{d}^{\mathrm{H}}\mathbf{d}}\right) \qquad \textbf{(17)}$$

The solution for the predicted noise reduction as given by (17) contains two important limitations. First, the optimum control force in (16) is not limited by the maximum force specifications of the actuator, i.e., (16) may specify forces well above the actuator's capability. Second, the coherence of the control signal with the sound field is not taken into account. As discussed in section Principal Component Controller, page 2, only the coherent part of the control signal is effective for noise control [11,28]. Methods of incorporating actuator force constraints and coherence effects in (16) will be described in the next two sections.

Actuator Force Constraints

Actuator forces can be constrained during operation of the LMS controller through the addition of a control effort penalty to the cost function equation, (15) [18].

$$J = \mathbf{e}^H \mathbf{e} + \mathbf{w}^H \mathbf{R} \mathbf{w} \qquad \textbf{(18)}$$

In (18) **R** is an arbitrary (*r*x*r*) weighting matrix and the term $\mathbf{w}^H\mathbf{R}\mathbf{w}$ represents a control effort penalty. The analytical solution for optimum control force now becomes

$$\mathbf{w}_{opt} = -\left(\mathbf{H}^H \mathbf{H} + \mathbf{R}\right)^{-1} \mathbf{H}^H \mathbf{d} \qquad \textbf{(19)}$$

A constrained minimization procedure can be used to solve (19) for the forces which produce the greatest noise reduction given a force limit. Although representative of what the actual control system would do, such an approach greatly increases the computation required because a penalty factor must be iteratively derived for every actuator in each new actuator set constructed during optimization. It has been demonstrated [15], that a uniform penalty matrix, i.e., one in which the values of **R** are equal, is adequate for purpose of finding an optimal actuator set as long as all calculated actuator forces are below the constraint limit. A uniform penalty value, r_u, can be approximated using an expression derived by Rossetti [18].

$$r_u = s_{\max} \frac{\sqrt{\mathbf{d}^H \mathbf{d}}}{w_{\max}} - s_{\min} \qquad \textbf{(20)}$$

In (20) s_{max} and s_{min} are the maximum and minimum singular values of the transfer function matrix, **H**, respectively. The force constraint limit is w_{max}. It has been observed that (20) produces a conservative value for r_u, that is, one in which the resultant forces are well below w_{max}. However, this doesn't seem to perturb the search from the optimal solution and once the optimum actuator set is found, the constrained minimization procedure can be used to arrive at a better prediction of the actual noise reduction, ignoring, of course, coherence effects.

Coherence in the Noise Prediction Solution

For given coherence, $\boldsymbol{\gamma}^2$, between the control signal and the primary source, the maximum, coherence limited, noise reduction is given by [7,29].

$$\Delta_{dB} = 10 \log_{10}\left(1 - \gamma^2\right) \qquad \textbf{(21)}$$

This solution ignores force limits. To best predict the noise reduction of an actuator set, the effect of coherence must be included in the constrained solution derived in the previous section.

Consider the primary sound field to be composed of coherent and incoherent parts. Assuming a

coherence of $\boldsymbol{\gamma}^2$, only the coherent parts of primary sound field can be controlled.

$$\mathbf{e}^{coh} = \mathbf{H}\mathbf{w} + \mathbf{d}^{coh} \qquad \textbf{(22)}$$

The coherent part of the primary sound field is $\mathbf{d}^{\text{coh}}$ and is given by (10). The associated coherent error signal is $\mathbf{e}^{\text{coh}}$. The solution for the optimum, constrained force is now

$$\mathbf{w}_{opt}^{coh} = -\left(\mathbf{H}^H\mathbf{H} + \mathbf{R}\right)^{-1}\mathbf{H}^H\mathbf{d}^{coh} \qquad \textbf{(23)}$$

Solving (23) for the optimum constrained force, $\mathbf{w}_{\text{opt}}^{\text{coh}}$ and substituting into (22) will produce the residual coherent sound field, $\mathbf{e}_{\text{min}}^{\text{coh}}$. The total sound field is the sum of the coherent and incoherent parts. The incoherent sound can be estimated by

$$\left(\mathbf{e}^{inc}\right)^2 = \mathbf{d}^{\mathrm{H}}\mathbf{d}\left(1-\gamma^2\right) \qquad \textbf{(24)}$$

The predicted noise reduction now becomes

$$\Delta_{dB} = 10\log_{10}\left(\frac{\left(\mathbf{e}_{\min}^{coh}\right)^2 + \left(\mathbf{e}^{inc}\right)^2}{\mathbf{d}^{\mathrm{H}}\mathbf{d}}\right) \qquad \textbf{(25)}$$

In the absence of constraint limits, the minimized coherent sound field, $\mathbf{e}_{\text{min}}^{\text{coh}}$, becomes zero by way of perfect noise reduction and (25) reduces to (21).

Actuator Location Survey

Obtaining an accurate characterization of the acoustic response due to each actuator is important to the optimization process. Methods to model the structural/acoustic response of an airframe at the fidelity needed for the optimization process are not available. An empirical approach is thus employed where an actuator is placed at each candidate location and the acoustic response sampled with an array of microphones. To avoid the time consuming process of installing actuators at each location, it was proposed that an actuator be clamped temporarily in position. The use of a single clamped actuator had the drawback that the relationship between the clamped actuator response and that of an installed actuator was in question. This relationship was further clouded given that, for the flight test, the actuators would be installed in pairs, one on either side of the ring frame, both acting in phase to increase in-plane force and to reduce tortional forces acting on the frame. A preliminary test was performed to validate the use of the single clamped actuator for the survey. These results are discussed in the section titled Actuator Authority, page 13.

The actuator is shown in Figure 3 mounted in the clamp. The clamp was able to be fitted to 82 locations on the 1900D frame as shown in Figure 4. Thirty two microphones were mounted as described in the section on Test Configuration. Transfer functions were obtained at the bpf and 4 higher harmonics.

Pressurization Effects

The actuator location survey was taken on the ground in an unpressurized cabin. The effects of cabin pressurization were a concern due to the changes in the structural/acoustic actuator transfer functions that might occur as the cabin stiffened under pressurization. If these changes were significant, they could invalidate the actuator location optimization. Recent work [30] has demonstrated that pressurization changes can have a pronounced effect on the performance and stability of an ASAC system. In [30] noise control predictions were obtained using a finite element model of an aircraft fuselage section for unpressurized and pressurized conditions. Both conditions use transfer functions obtained in unpressurized conditions, see **Table II**. The 1st harmonic exhibits some loss of control capability with pressurization, but remains stable. The 2nd and higher harmonics, however, all become unstable and uncontrollable. This is a strong indication that an actuator set optimized with ground-based transfer functions will not perform as predicted once in-flight, especially at the higher harmonics. To increase confidence in the actuator location optimization, it may be necessary to acquire the candidate transfer under pressurized conditions, or even in flight.

Multi-Frequency Optimization

Multi-frequency actuator location optimization was accomplished using total noise reduction as given by the weighted sum over the frequencies of interest as the search cost function.

$$J_{tot} = \sum_{i=1}^{n} a_i^2 J_i \qquad \textbf{(26)}$$

The parameters, a_i, are defined according to the weighting method used.. Three weighting methods were evaluated: linear, dBA and loudness level as shown in Figure 5, Figure 6, and Figure 7 respectively. It was originally intended to design the control system for the blade passage frequency and its first 4 harmonics. Loudness level weighting indicated there would be no subjective benefit from controlling the higher harmonics. The linear (unweighted) results are similarly dominated by the fundamental. The A-weighted curve shows that the 4th and 5th harmonic may not be worth controlling, but the 2nd and 3rd harmonics contribute to over half the noise reduction. For these reasons the optimization and control was performed using both the linear (unweighted), and A-weighted cost functions.

PC Optimization

The noise control algorithm is implemented in the principal component domain as described in the section, Principal Component Controller. One of the features of the PC controller is that increased stability and performance can be achieved by not controlling the higher order principal components which are associated with smaller singular values and higher control forces. This functionality can be simulated by using the PC domain noise prediction equations as given by equations (10) through (12) to compute the optimization cost function. However, this adds a great deal of computational overhead as the singular value decomposition of each candidate actuator set must be taken before the associated noise reduction (cost function) is computed.

An alternative approach has been used whereby the actuator force constraints are purposely set below maximum force to bias the optimization procedure towards concentrating as much of the primary source power in the low order, most efficient principal components as possible. As an example consider a 12

actuator, 32 microphone control system. Selecting a random set of actuators from the database of 82 possible locations results in singular values as shown in Figure 8. This shape for the singular values is typical, regardless of optimization. The larger, low order, singular values have greater capacity for controlling the acoustic power that is mapped into their respective domains. The fraction of the total primary source acoustic power in the principal components for the random actuator set are shown in Figure 9. This system will not achieve good noise reduction because too much acoustic power is concentrated in the higher order PCs which are either uncontrollable or difficult to control (due to small singular values). A set of actuators optimized using nominal constraints improves the design by shifting more acoustic power into the 12 controllable PCs, Figure 10. Further improvement can be achieved by overly constraining the maximum actuator force as shown in Figure 11. Here the majority of the acoustic power is concentrated into the first few PCs, matching the authority available through the larger singular values.

Optimization Results

The optimization results are presented in three sections. The first section describes a sensitivity analysis which evaluates the consistency of the actuator survey data. The second section discusses the relationship between the number of actuators and noise reduction. Finally, the third section describes the process by which the optimized actuator set was derived.

Sensitivity Analysis

It has been observed during previous tests on NASA's Composite Cylinder [5,31] that the performance of an optimized actuator set can vary widely with small changes in the actuator transfer functions. Figure 12 shows the sensitivity of the predicted noise reduction obtained with an optimum set of actuators on the Composite Cylinder when the magnitude and phase of the actuator transfer functions are varied ± 5% for 500 trials. Notice that the mean of the distribution is about 6 dB below the noise reduction predicted for this set of actuators with the bulk of the distribution spreading over several dB. This indicates that small errors or anomalies in acquiring the actuator transfer functions can have a large impact on optimization results and thus lower the confidence that the predicted noise reduction of an optimized set will be achieved.

The 1900D actuator set has been found to be insensitive to transfer function variation, see Figure 13. Here, the noise reduction for the optimum set is –14.2 dB, just 0.5 dB from the mean of the distribution with most of the distribution lying within 1 dB. It is thus highly likely that the optimum set will perform as predicted (ignoring pressurization effects as discussed earlier).

Number of Actuators vs. Noise Reduction.

The number of actuators required for the control system was roughly estimated to be 24 actuator pairs (see section, Actuator Authority, page 13). Once the actuator transfer functions became available, a better estimate was made by constructing and evaluating optimum sets of several sizes. Figure 14 shows predicted noise reduction for optimized actuator sets of 1 to 24 actuator-pairs. It can be seen from the figure that the noise reduction obtained per added actuator-pair decreases after 12 actuators. Over 12 dB of attenuation is achieved with 12 actuator pairs and just over 14 dB at 24 actuator-pairs. The 12 channel system delivers 85% of the noise reduction with 50% of the actuators and may be considered a preferred design. The 12 channel system is also a better test of the optimization procedure's capability in that the design leaves less room for error compared to the added redundancy of the 24 channel system. During the flight test, 2 configurations were tested, a full configuration using all (21) available actuator channels

and a reduced configuration with 12 channels.

Final Design

The actuator set used in the noise control flight tests was selected using an overly constrained optimization (see section, PC Optimization) over the first 3 harmonics. Both 21 actuator-pair and 12 actuator-pair configurations were derived for the planned flight tests. The 12 actuator-pair configuration was modified slightly so that it was a subset of the 21 actuator-pair set. **Table III** contains the frame-bay locations for both the 21 actuator-pairs and the 12 actuator-pairs. Figure 15 shows the numbering of the bays on the 1900D as viewed facing forward in the cabin. Figure 16 shows all 21 locations in a view where the frames are unwrapped with bay #1 on the port or left side. The 1st frame is closest to the cockpit, just behind the door, and is placed at the top of the figure.

The predicted noise reduction is listed in Table IV for linear and A-weighted cases. Although the A-weighting produces a smaller overall noise reduction figure, the value of the 1st harmonic reduction is identical to the linear case and the values of the 2nd and 3rd harmonics increase only slightly. This is further evidence of the dominance of the 1st harmonic.

The actuator forces and primary source principal component distributions for the three harmonics are plotted in Figure 17 through Figure 22. Actuator force is presented in terms of the voltage applied to the actuator. During preliminary testing, it was found that a single actuator would tend to produce distortion if operated much above 7.5 Vrms. To model an actuator pair, the total force summed across the three harmonics was limited to 15 Vrms. The highest component of force for an actuator-pair was 11.6 Vrms in the 2nd harmonic, versus 9.1 Vrms in the 1st and 8.5 Vrms in the 3rd. The total force is taken as the square root of the sum of the squares of the forces across the 3 frequencies as it is desired to limit the power dissipated in the actuator. The total force for the actuator-pairs is shown in Figure 23. The maximum actuator force is 14.7 Vrms.

The noise controller used only the first 18 principal components due to processing limitations in the DSP controller. Because of this, it was important to concentrate as much of the primary source in the first 18 principal components as possible. The principal components of the first harmonic are well constructed. The 2nd harmonic PCs are good, while the 3rd harmonic PCs are only fair. The poor fit in the higher harmonics may be due to the placement of the microphones. Although the singular value decomposition creates an orthogonal coordinate system, the system is not guaranteed to relate to physical modes of the structural acoustic system, especially if the mode structure is not sampled adequately. If the physical modes are not present in the primary source PCs, then it can be expected that the actuator responses may not map well. The section on Interior Noise Field will look more closely at this problem.

The Raytheon 1900D

The Raytheon/Beech 1990D, Figure 24, is one of the most widely used turboprop airliners in the industry. The aircraft can carry 19 passengers 2900 km at a maximum cruise speed of 533 kph. The interior cabin is shown in Figure 25. Other aircraft specifications are listed in Table V. The 1900D has a 4 blade propeller with a blade passage frequency (bpf) of ~103 Hz. The twin engines are phase locked through a synchrophaser at the shaft speed of 25.8 revolutions per second (rps).

Interior Noise Field

The interior noise field was sampled by the Naval Research Lab in preparation for a near field acoustic holography study [32]. Although this data was not available for this flight test, it serves as a useful tool in understanding the noise environment on the 1900D. Figure 26 shows the NRL microphone rig installed in the 1900D. The cabin had the trim panels and seats removed. Figure 27 is a detailed drawing of the rig showing microphone placement. A dataset was taken every 16.5 cm along the axis the cabin interior. If the pressure readings taken from the microphones located around the circumference of the rig (from **A** through **I** in Figure 27) are arranged in a row and each acquisition is stacked one on the other, a map of the acoustic pressure along the interior borders of the airframe can be constructed as shown in Figure 28. Figure 29 shows the area of the fuselage over which the scans were taken in the correct orientation with respect to Figure 28. A row of pressure data starts at **A**, in the center of the floor, goes to the port side-wall, **B**, proceeds up the port side-wall through **C** and **D** to the top center of the fuselage, **E**, then proceeds down the starboard side to the floor at **H** and back to the center of the floor at **I**. The top of Figure 28 corresponds to the forward area of the cabin.

From this data it is clear that the 1st harmonic contains a great deal of energy in the propeller plane. The light blue lines in Figure 28 are the lines along which the controller's microphones were installed. In the case of the 1st harmonic, it would have been difficult not to intersect the anti-nodes. Similar scans of the 2nd and 3rd harmonics are shown in Figure 30 and Figure 31 respectively. As can be seen in the figures, the controller's microphone array does not adequately sample the sound fields for the 2nd and 3rd harmonics. This may have contributed to the optimization's inability to construct an actuator set that coupled well to these harmonics as discussed in the section PC Optimization.

The spectrum taken for a microphone in the forward cabin in the propeller plane is shown in Figure 32. The 1st harmonic attains nearly 110 dB SPL and is at least 10 dB above the higher harmonics. The noise floor is below 70 dB thus providing a range of 40 dB for possible reduction of the 1st harmonic. However, maximum noise reduction is limited by the coherence between the noise field and the reference used by the controller. An estimate of the maximum obtainable noise reduction can be made using the coherence of the primary field with the synchrophase signal that was used as a reference in the controller. Figure 33 shows the coherence of the microphone with the synchropase signal over the frequency range of 50 to 550 Hz. Table VI lists the harmonic frequencies with associated coherence and maximum noise reduction possible. It can be seen that if the controller maintains perfect synchrony with the engines, then a maximum of 20 dB noise reduction is possible on the 1st harmonic.

Test Configuration

A list of the flight test equipment is given in Table VII and a block diagram of the system is shown in Figure 34. The control system used 32 microphones and 21 actuator-pairs. The controller, conditioners, amplifiers and digital tape recorder were arranged in 2 racks as shown in Figure 35 and Figure 36. The trim panels and seats were not installed in the aircraft.

Controller

The controller consisted of a rack-mounted computer with digital signal processor (DSP), I/O and synchrophase interface. The DSP board held two TMS320C40 processors. The DSP processors communicated over a proprietary bus to the 3 I/O boards. Each I/O board had 16 input and 8 output channels. The synchrophase interface converted the propeller shaft synchrophase signal into a TTL compatible signal which was then routed into a DSP interrupt. In the DSP, an internal timer was

synchronized to the interrupt signal by a software phase-locked loop algorithm. The PLL set the internal timer to operate at a multiple of 48 times the interrupt rate to establish a sampling rate of approximately 1238 Hz that would be directly proportional to the propeller shaft speed (~25.8 rps). Filters on-board the I/O boards were set to 723 Hz and provided –18 dB roll-off per octave.

Acquisition

The microphones were Modal Shop 130B10 with 130P11 preamplifier. Microphone specifications are shown in Table VIII and typical calibration curves for the 130B10 are shown in Figure 37. The microphones were clamped to the ring frames and protruded into the cabin about 20 cm from the skin as shown in Figure 38. The microphones were uniformly distributed, 4 mics on a ring frame (as shown in Figure 39) with the lower and upper microphones roughly corresponding to seated and standing head heights, respectively. The 8 frames closest to seat locations were instrumented. Twelve accelerometers where installed on the 1900D ring frame adjacent to the actuators to sample frame vibration during testing. The accelerometers were of type PCB A352B65 with approximately 105 mV/g sensitivity. The microphones and accelerometers were connected to PCB 584 signal conditioners. The 584 provides 16 channels of ICP® power and conditioning. No filtering or gain ranging was done in the 584. All sensors plus the master and slave synchrophase signals were recorder on a Metrum RSR 512 digital tape recorder.

Actuation

The actuators were of type Motran IFX 15-100. These are inertial actuators made especially for installation on an aircraft ring frame. A sketch of the IFX 15 is shown in Figure 40 and specifications for the actuator are summarized in Table IX. Typical response curves are shown in Figure 41 and Figure 42. The compact size and high force was achieved by the use of Tungsten for the mass. This greatly increases actuator cost, but, as will be shown later, these high forces may not be necessary in practice, thus opening the door for cheaper designs.

The actuator resonant frequency (95 hz) was tuned to be just below the 1900D blade pass frequency (103 Hz) to avoid the steep phase change that occurs around resonance. The coil resistance (7.5 Ω) was chosen to be compatible with the Rane MA 6S multi-channel audio amplifiers that were used to power the actuators.

Actuator Authority

To provide a basis for estimating the number of actuators that would be needed in the control system, a preliminary evaluation of the actuator's noise control authority was made on the 1900D in a ground test. Three versions of the actuator with resonant frequencies of 95, 180 and 267 Hz were installed on the 1900D's ring frame in the prop plane. Ten microphones were placed around the circumference of the interior (5 microphones per ring frame) to measure the sound field produced by the actuators.

The actuators can be installed either singly or in pairs on the aircraft frame. The relative performance of single versus paired actuators was measured and is shown in Figure 43. The vertical dashed lines mark 5 harmonics of the bpf and are labeled with the dual, single and difference pressures. As can be seen, an actuator pair provides close to 6dB more sound pressure for the first 3 harmonics. The responses of a bolted versus a clamped actuator are compared in Figure 44 to illustrate the effect of using a clamped actuator during the actuator location survey. The clamped actuator response closely follows that of the bolted actuator except for around 150 Hz where a clamp resonance comes into play. Although the resonance does not interfere with the bpf and its harmonics the clamp was subsequently redesigned to

eliminate the resonance.

Figure 45 shows the average magnitude of the sound pressure for the 3 actuators tuned to 95, 180 and 267 Hz when the actuators are driven singly at full power at 104, 208 and 312 Hz respectively. To accommodate the time necessary for manufacturing, it was necessary to estimate the number of actuation channels needed for the control system before the optimization analysis could be run. The estimate was based largely on an authority argument which assumed that the control effort would be dominated by the first harmonic. Taking into consideration Figure 28, it can be seen that the sound field can easily approach 115 dB in places. From Figure 45, a single actuator would be 20 dB below the 115dB target and a dual actuator 15 dB below. Assuming a conservative 3 to 4 dB gain in output per doubling of actuators, an estimate can be made that 16 to 32 actuator pairs are needed for control. The control system was designed for up to 24 actuator pairs as a compromise.

Noise Control Results

The noise control system was tested during two flights conducted in the morning and afternoon of August 12, 1998. The synchrophaser was not working during the morning flight, which greatly reduced the coherence between the synchrophase signal from the port engine and the interior noise field. As a result, the noise reduction levels obtained during this flight were disappointing. Fortunately, the synchrophaser was repaired before the afternoon flight, and good noise reduction results were obtained on that flight. Most of the discussion here will focus on the second flight, although data from the first flight will be mentioned briefly to illustrate the impact of low coherence on control system performance.

The section begins with a description of the test procedure. The measured data are discussed next, including: coherence data for the control system, properties of the transfer function matrices, and noise reduction results for various test configurations.

Test Procedure

The two flights followed similar flight profiles with different test points obtained during each flight. The first flight was originally intended to verify stable operation of the control system while controlling individual harmonics of the bpf. Assuming all went well on that flight, the controller would then be used for simultaneous control of multiple harmonics during the second flight. Unfortunately the results from the first flight were quite disappointing because of the inoperable synchrophaser, but nonetheless the basic plan for the two flights was followed.

The approximate flight profile for both flights is illustrated in Figure 46. The flight began with a climb to a cruising altitude of 15000 feet, at which point the pilot reduced the engine speed from the nominal engine speed of 1550 rpm to 1440 rpm. This shifted the propeller blade passage frequency and its harmonics away from their normal operating frequencies, thereby allowing the control system to measure the transfer functions between actuators and error sensors at the normal operating frequencies. The transfer functions were measured by exciting an individual actuator pair with one of the first three harmonics of the normal bpf while recording the microphone responses.

Once the system identification was completed, the pilot restored the engines to their normal operating speed and the noise reduction tests were started. The test points obtained during the two flights are listed in Table X. The first column in the table gives the run number for the test points; these numbers will be used in the subsequent discussion of the results. The next two columns contain a description of each test point and the approximate length in minutes of each test. The notation bpf and 2bpf denote the blade

passage frequency and its second harmonic, respectively. All of the test points listed in the table, with the exception of run 1.2b in the first flight, were conducted with the control system synchronized to the left (portside) engine. The total elapsed times from the start of the system identification procedure to touchdown for flights 1 and 2 were 97 min and 79 min, respectively.

Before each noise control test, the controller's effort constraints were initialized to very conservative values. After the control system appeared to be operating in a stable fashion, a human operator slowly reduced the constraints, thereby allowing the control system to more aggressively reduce the microphone responses. This procedure resulted in very long controller convergence times, which will be apparent in the noise reduction plots.

Coherence Results

The coherence between the reference signal and the primary noise field determines the maximum possible noise reduction in a feedforward control system [7,29]. Experimentally measured values of the coherence are discussed here, including comparisons for synchronized versus unsynchronized propellers, and single engine versus two engine flight conditions.

The reference signal was generated on the DSP synchronously with the synchrophase signal taken from the port engine. One would therefore expect relatively good coherence between the reference and the noise field created by the portside propeller. Because the interior noise field contains contributions from the port and starboard propellers, the coherence may be reduced, dependent on the precision of the aircraft's synchrophaser. Another factor contributing to reduced coherence may be the presence of uncorrelated effects such as aerodynamic buffeting.

For these measurements, the path from the internal reference to the response of each microphone was treated as a single input/single output system. Denoting the reference signal input by the symbol x, and the response of a single microphone by y, the coherence at the discrete frequency f_k was computed as

$$\hat{\gamma}_{xy}^2(f_k) = \frac{\left|\hat{G}_{xy}(f_k)\right|^2}{\hat{G}_{xx}(f_k)\hat{G}_{yy}(f_k)} \qquad \textbf{(27)}$$

where $\hat{G}_{xy}(f_k)$ is the estimated cross-spectral density, and $\hat{G}_{xx}(f_k)$ and $\hat{G}_{yy}(f_k)$ are auto-spectral density estimates. The density functions were estimated using the procedures described in Sections 11.5 and 11.6 of [33].

The primary noise field in the aircraft is not necessarily stationary, which complicates accurate estimation of spectral density functions. Long records of time domain data are useful for reducing variance in the estimate due to random noise, but if the characteristics of the signal change over the course of the record, the resulting estimate will be biased. As a compromise between variance and stationarity considerations, the spectral density functions were estimated by averaging 15 data records of 1200 points each. The records were nearly consecutive in the time domain, but the time required to upload each 1200 point record from the DSP to the computer prevented continuous records from being accumulated. As a result, no overlap was used between adjacent records when computing the spectral density estimates. Assuming a nominal engine rate of 25.8 rps, the sample rate was

1238.4 Hz = (25.8 rps) * (48 samples/revolution).

A 1200 point data record contained just under one second of data, while the ensemble of records contained approximately 15 sec of data, including the very small time intervals for uploading . The frequency spacing of the resulting spectral density estimate was

1.03 Hz = (1238.4 samples/second) / (1200 samples).

Figure 47 shows the coherence between the reference and the microphone responses, as measured during the second flight before run 2.5a (see Table X). The x-axis denotes the microphone channel ranging from 1 to 32, except for channel 7 which was inoperable during the tests and therefore is not plotted. The coherence is shown at the first three harmonics of the blade passage frequency, which are denoted as bpf, 2bpf, and 3bpf. The coherence values are generally high, and show a slight drop with increasing harmonic number. One would expect to see greater microphone to microphone variation at the higher frequencies where the wavelengths are shorter.

The relatively high coherence values shown in Figure 47 can be contrasted with those in Figure 48, which were measured during the first flight when the synchrophaser was inoperable. During this first flight, the two propellers were essentially acting as independent noise sources at the blade passage frequency and its harmonics. Because the reference signal was only synchronized to one of the engines, the primary response due to the other engine acted as an incoherent noise source, greatly reducing the overall coherence values.

The coherence was also measured with one engine running at a reduced speed, thereby removing its contribution to the primary noise field at the first several harmonics of the normal blade passage frequency. These data were measured during a preliminary flight test in May of 1998, and were computed using the procedure described above. The coherence with only one engine running at the normal operating speed is shown in Figure 49, while the coherence with both engines running at the normal speed is shown in Figure 50. There is a slight drop in coherence when the second engine is added, but the change is very small, and is certainly within the range of experimental error. Note that the data in Figure 47 and Figure 50 were measured several months apart but represent the same operating conditions, and therefore indicate some of the variability in the primary noise field.

System Identification

A feedforward control system requires a model of the transfer functions between control actuator outputs and error sensor inputs to correctly update the control filter weights. These transfer functions can be measured in a number of ways, either on-line while the controller is running or off-line, as was done for the current flight test. The conditioning of the transfer function matrices at the three bpf harmonics is discussed here.

The transfer functions were computed in-flight before the controller was turned on, with the engines operating at a reduced rpm. The measurements were done with one actuator and at one frequency at a time to maximize the coherence from the actuator input to each microphone response. Assuming the time history of the input to the i^{th} actuator is denoted by x and the response of the j^{th} microphone is y, the $(i,j)^{th}$ element of the transfer function matrix was computed as

$$H_{ij}(f_k) = \frac{\hat{G}_{xy}(f_k)}{\hat{G}_{xx}(f_k)} \qquad \textbf{(28)}$$

The quantities $\hat{G}_{xy}(f_k)$ and $\hat{G}_{xx}(f_k)$ are cross-spectral and auto-spectral density function estimates, respectively. The density functions were measured using the same data record length and bin spacing that were used for the coherence measurements described above.

The condition number of the transfer function matrix at each frequency from ground test and the morning and afternoon flights, is listed in **Table XI**. The condition number is the ratio of the largest to the smallest singular value of the matrix and indicates the degree of ill-conditioning in the matrix. The condition number at the first harmonic in both flights is very high, and indicates some ill-conditioning in the transfer function matrix. The ground based condition number is much lower. From the theory of feedforward adaptive control algorithms [11,17], a high condition number means the convergence times for the last PC will be much greater than for the first PC. Depending on the primary noise field, this could also mean the last few PCs will require much greater control efforts than the first PCs. The condition numbers at the second and third harmonics of the bpf are not as high, and as a result there shouldn't exist such a wide discrepancy between the convergence times of the first and last PCs at this frequency.

It should be noted than in a normal filtered-x LMS controller, the high condition number at the first harmonic would have a negative impact on the convergence of the control system, but its effect on the PC-LMS algorithm is not as pronounced. The PC-LMS algorithm provides a means to set different step sizes for each PC, and thus PCs with very long convergence times can be given larger step sizes to accelerate their convergence.

Table XII lists the infinity norms of the transfer function matrices, where the infinity norm is defined as the maximum singular value of the matrix. This number gives a rough indication of the gain of the control system at each frequency, since the transfer function matrix describes the microphone responses when a unit amplitude sine wave is input to a control actuator. As with the condition numbers there is a general similarity between the infinity norms measured during the morning and afternoon flights. This is a very crude metric indicating the properties of the transfer function matrices did not change excessively between the two flights. However, the difference between the in-flight and ground-based infinity norms suggests a significant change in conditions.

The in-flight values in Table XII indicate the gain of the control system was at least three times greater at the first harmonic than at the higher harmonics. This indicates the reduced authority of the control system at the higher harmonics, and is likely a result of the mechanical properties of the control actuators. The natural frequency of the actuators was designed to be 95 Hz, which is close to the norminal bpf of 103 Hz, and thus the response of the actuator would be expected to drop off significantly at 203 and 309 Hz, the frequencies of the second and third harmonics.

First Harmonic Results

We begin the discussion of noise reduction results with measured reductions of the first harmonic of the blade passage frequency, at approximately 103 Hz. As in all of the noise reduction tests, the control system was operated very conservatively; constraints were set high initially, and were slowly reduced after the control system appeared to be stable. This resulted in long convergence times, which were acceptable for these tests since it was more important to demonstrate predictable, consistent operation of

the control system than rapid convergence.

The average sound pressure level (SPL) over the microphone array before control was applied is shown in Figure 51. These data were measured during run 2.1a during the afternoon flight, when the synchrophaser was operational. Note that microphone 7 in the 32-microphone array was not working, hence the results here are averaged across the 31 working microphones. The SPL of the first three harmonics of the bpf in the plot are 105, 97, and 88 dB, respectively. The tone at approximately 160 Hz is associated with the environmental control system on the aircraft and was not targeted by the noise reduction system during these tests. Single frequency control of the bpf was tested during run 2.1a. A time history of the SPL of the blade passage frequency after control was turned on during run 2.1a is shown in Figure 52. The solid line shows the average SPL measured at approximately 1 second intervals during the 6.75 minute test. The dashed line and the dotted line are predictions of the noise reduction that take into account the control effort constraints; the dashed line also factors in the measured coherence, while the dotted line assumes unity coherence. The effort constraints were incrementally reduced during the test, hence the "stairstep" appearance of the predicted noise reduction. The average SPL after 6.6 minutes is shown in Figure 53.

The results demonstrate both dramatic noise reduction and consistent, predictable performance by the control system. The bpf was reduced by nearly 15 dB, averaged across all 31 microphones, six minutes after the control system was turned on. The measured reduction closely matches the prediction that factored in both the coherence and the control effort constraints, indicated by the dashed line in the Figure 52. The SPL decreased in a consistent fashion during the test, and appeared to be leveling off towards the end of the test.

Time histories of the peak voltage inputs to the 21 control channels are shown in Figure 54. These voltages were computed on the DSP and therefore represent the outputs of the digital to analog (D/A) converters before amplification. The D/A's had a maximum output of ± 10 Volts, and the control system was programmed to automatically shutdown when an actuator control signal exceeded this level. The voltage traces in the figure indicate an actuator control signal exceeded the limit, which ended the noise reduction test.

A comparison of microphone responses before and after control is shown in Figure 55 and Figure 56. The microphones are located at intersections of the lines in the figure; a level for the malfunctioning microphone was computed by interpolating between neighboring microphones. Comparing the levels in the before and after plots illustrates that significant noise reduction was produced throughout the aircraft interior.

Further evidence of the predictable performance of the control system is provided by plotting the estimated versus the measured control inputs, in terms of the principal components of the control system. The control inputs were computed in terms of the PCs of the control system and were then transformed into actuator inputs. Time histories of the predicted versus the actual inputs to the first four PCs are shown in Figure 57.The predictions were computed using (11) and are indicated by the dashed lines. The predicted and measured values show good agreement, although the predictions are slightly low for PCs two and three. The curves indicate these PC inputs had fully converged by ~ 4 minutes into the test.

Although the afternoon flight produced more significant noise reduction than the morning flight, it is still useful to examine results from one of the morning tests. The first harmonic of the bpf was controlled during run 1.1a. As previously discussed, the coherence between the internal reference signal and the primary noise field was very low during the first flight because the port and starboard propellers were not

exactly synchronized with one another. A time history of the reduction in the bpf is shown in Figure 58. As in Figure 52, the dashed line shows the predicted noise reduction, including both effort constraints and measured coherence, while the dotted line assumes unity coherence. The measured reduction contains an oscillatory component due to beating between noise generated by the unsynchronized propellers. Approximately 5.5 minutes after the controller was turned on, there was a pronounced reduction in the amplitude of the beating, when the convergence rate, μ, was increased. This illustrates the ability of the control system to track cycle-to-cycle variations in the primary noise field.

The importance of high coherence is indicated by the large difference between the two noise reduction predictions. If the coherence had been unity between the reference and each microphone, the primary would have been reduced by over 20 dB, but the true coherence limited the reduction to just under 5 dB. The mismatch between the two predictions also serves to emphasize the importance of including the coherence in any offline prediction of the noise reduction performance of a control system.

Second Harmonic Results

The second harmonic of the blade passage frequency was controlled during run 2.6a of the afternoon flight. The reductions were much smaller than for the first harmonic, and the results indicate this was due to a limitation of the actuator authority, not due to low coherence.

The time history showing the measured reduction in the SPL of the second harmonic of the bpf is plotted in Figure 59. The maximum reduction was slightly over 4 dB. There is relatively little difference between the predicted noise reduction computed with and without the measured coherence, as indicated by the dashed and dotted lines, respectively. As with the results from run 2.1a during the afternoon flight, there is generally good agreement between the dashed line and the measured noise reduction, after the control system had converged. The similarity between the two predicted noise reduction curves indicates that the coherence was not a limiting factor during this test.

The maximum voltage inputs to the control actuators are shown in Figure 60. A single actuator exceeded the ±10 Volt limit, stopping the control system 3.25 minutes into the test. It should be noted that the control effort constraints were all reduced to zero during this test in an attempt to improve the noise reduction performance.

The predicted and measured control inputs to the first four PCs are shown in Figure 61 where the predictions are indicated by the dashed lines. As with control of the bpf, there is good agreement between the actual performance of the control system and the predicted performance, and the inputs to the first four PCs appeared to have converged to their final values during the test.

Since neither the coherence nor the effort constraints were limiting the noise reduction performance, and because the control system appeared to be doing exactly what the predictions said it would do, we conclude that the coupling of the actuator array to the primary noise field must have been insufficient at this frequency to produce good noise reduction. Poor coupling could be due to poor placement of the actuators and/or the microphones. These factors become more important at higher frequencies where the wavelengths are shorter. Lack of actuator authority could also have been due to the reduced output of the control actuators, which were tuned to 95 Hz, well away from the 206 Hz nominal frequency of the second bpf harmonic.

Multi-Frequency Results

We next discuss the results of two tests, conducted during the afternoon flight, in which the first three harmonics were controlled simultaneously. The goal of the first test (run 2.1b in Table X) was to minimize a linear summation of the levels of the three harmonics. From the uncontrolled harmonic levels shown in Figure 51, this amounted to reducing the bpf first, then the second harmonic, and then applying any remaining control authority to the third harmonic. The goal of the second test (run 2.3a in Table X) was to minimize an A-weighted summation of the harmonic levels. This amounted to reducing the third harmonic, followed by the second, and then the bpf. Because of the controller's low authority at the second and third harmonics, the end result of these two tests was similar; small reductions were obtained at the two higher harmonics, because most of the control energy was spent where it was most efficient, on the bpf.

The results of each test are summarized in five plots here. Three of the plots show time histories of measured and predicted reductions at the three harmonics; one plot shows actuator input voltages; and one plot shows the convergence of a cost function consisting of either a linear or A-weighted summation of the SPL at the three harmonics.

Linear Cost Function

Measured and predicted reductions of the first three harmonics, from run 2.1b, are shown in Figure 62 through Figure 64 . The test was approximately six minutes long, and produced noise reductions at the first three harmonics of 10.2 dB, 3.3 dB, and 1.6 dB, respectively. The measured noise reductions at the three frequencies agree well with predicted reductions. Time histories showing the reduction in a linear and an A-weighted summation of the three harmonics are plotted in Figure 65. The linear cost was reduced by slightly more than 8 dB during the test.

The actuator input voltages are shown in Figure 66. The inputs to two actuators exceeded the voltage limits of the D/A converters at the end of the test.

A-weighted Cost Function

Figure 67 through Figure 69 show reductions in the first three harmonics when the cost function consisted of an A-weighted summation of the harmonic levels. Due to the inability of the control system to achieve good noise reduction in the higher harmonics, there are few differences between these results and those obtained from run 2.1b described in the preceding section. Measured reductions in the first three harmonics of 9.9 dB, 2.3 dB, and 2.6 dB, respectively, were obtained. Compared to the results from run 2.1b, there was an improvement at the third harmonic, from 1.6 dB to 2.6 dB of reduction, but this came at the expense of the second harmonic, which was only reduced by 2.3 dB in this test.

A time history of the cost function reduction is plotted in Figure 70. The A-weighted reduction of the three harmonics was just over 4 dB, which is nearly identical to the reduction that was obtained in run 2.1b. The linear reductions were also nearly equal for the two tests. Note that approximately 5.5 minutes into the test it became clear that no appreciable reduction could be obtained at the second and third harmonics, so the effort constraints on the first harmonic were relaxed. This is the reason for the sudden increase in the reduction of the blade passage frequency evident in Figure 70.

The time histories of the maximum actuator input voltages are shown in Figure 71. The input to one actuator exceeded the limit, shutting down the control system at ~ 6.5 minutes.

Control During Descent

In run 2.7a, a multi-frequency control test was performed during descent through landing to study the robustness of the control system to altitude changes. It is well known that the stability of a filtered-x type of controller, upon which the PC-LMS algorithm is based, depends on the accuracy of the transfer function matrix between actuators and sensors. This matrix was measured in-flight at cruising altitude where the aircraft cabin was pressurized. As a result this test provided a simple means to assess whether or not these transfer functions were sufficiently accurate for the control system to remain stable on the ground when the aircraft was unpressurized.

The test lasted 17 minutes, the first 8 of which took place at normal cruising altitude at normal engine torque levels. After 8 minutes, the pilot throttled back the engines, which greatly reduced the primary noise field. In an attempt to re-establish a 0 dB reference point for the control system the control filter weights were reset to zero, and this reset operation will be apparent in the plots discussed here.

Reductions in the first three harmonics are shown in Figure 72 through Figure 74. It is important to note that the noise reductions were computed relative to the primary noise field at 0 minutes and are, therefore, incorrect when the engine torque is reduced (thereby reducing the primary noise field). Nonetheless, the values indicate the control system remained stable for the duration of the test. The large variation apparent near the end of the test was caused by the feathering of the propeller blades, which temporarily increased the interior noise levels. The predicted noise reductions are also plotted, and generally agree well with the measured values for the first eight minutes.

The time histories of the maximum actuator input voltages are shown in Figure 75. The effect of resetting the weights eight minutes into the test is apparent in this plot. Note that just before the eight minute mark, the weights were maintained close to but still below the limits of the D/A hardware. This demonstrates the effectiveness of the control effort constraints for maintaining steady operation of the control system.

Reduced Configuration

The optimization results indicated that the potential existed for a reduced system configuration to achieve 85% of the noise reduction of the full-up system. An 8 microphone by 12 actuator system was tested in run 2.5a. The 8 microphones were those at head height in the first 4 rows of the cabin. This would demonstrate the effect of controlling only the area in the prop plane on the rest of the cabin. The positions of the 12 actuators are shown in Figure 76.

The uncontrolled and controlled sound fields are shown in Figure 77 and Figure 78, respectively. The overall sound level is reduced about 5 dB. There is no indication of global control, the sound field being reduced for the most part only at the 8 controlled microphones. At the 8 controlled microphones the noise reduction was approximately 10 dB.

The optimization procedure predictions are compared with those actually achieved in Table XIII. Clearly the system did not perform as expected for all 3 harmonics. This is further indication of the effect of cabin pressurization on the structural acoustic system. As mentioned earlier, the reduced configuration has little margin for error and is thus a good benchmark for the optimization procedures predictions. These results emphasize the need for good noise reduction predictions if optimization is to be used to design lower cost control systems.

Discussion

The PC-LMS controller performed extremely well. The PC domain perspective of the control system is both informative and instructive. The ability to adjust the convergence rate and effort penalty for each principal component in each frequency provides comprehensive versatility. The only drawback to this kind of implementation is the difficulty in defining the correct settings for all the parameters (the 3 frequency, 18 PC controller had 108 parameters). During the flight test a human operator slowly relaxed the effort penalties until maximum noise reduction and drive force were reached. In practice these terms would either be computed ahead of time or set adaptively in real time. For example, an outer loop controller, possibly in fuzzy logic, could be implemented to accomplish this task.

At first glance, the optimization procedure seems to have done a fair job of predicting the controller's performance during the multi-frequency, full-up test, runs 2.1b and 2.3a, see Table XIV. The predicted overall linear reduction is 12.9 dB while that achieved is 8.1 dB. However, the poor performance in the second and third harmonics becomes evident in the A-weighted numbers with a predicted reduction of 10.8 dB and an achieved of 4.4 dB.

A factor contributing to the loss of performance was that the in-flight transfer functions had changed enough so that the primary source principal components had shifted. Figure 79 and Figure 80 are the primary source principal components for the bpf for ground and flight transfer functions. Note how the acoustic power is shifted to the higher order PCs where actuator authority is reduced. The overall effect might best be appreciated by viewing Figure 81 and Figure 82 which are plots of potential noise control for each PC in dB versus the fraction of maximum control power necessary for both the ground and flight cases. The potential noise control is derived by cumulatively summing the primary source PCs.

$$NC_i = 10\log 10\left(1.0 - \frac{\sum_{j=1}^{i} p_j^2}{\sum_{j=1}^{18} p_j^2}\right)\{i = 1\cdots 18\} \qquad \textbf{(29)}$$

Where NC_i is the potential noise reduction in dB for the ith PC. The fraction of maximum control power is found by normalizing the cumulative control power to the maximum power.

$$CP_i = \frac{\sum_{j=1}^{i} \left(v_j^{pred}\right)^2}{CP_{\max}}\{i = 1\cdots 18\} \qquad \textbf{(30)}$$

Where CP_i is the control power fraction, CP_{max} is the maximum control power and v^{pred} is the computed control force from (11). Notice that, for the ground case, the fundamental's 13.5 dB reduction is achieved at 25% power. For the in-flight case, the 10.2 dB figure is not reached until close to 50% of the available actuator power is consumed. In multi-frequency control, the loss of authority snowballs because if more power is used to reduce one frequency, less is available at another, where loss of authority has already taken a toll.

Despite the loss of control authority, the control system achieved good noise reduction at relatively low power levels. In Figure 52, the bpf is shown to be reduced about 12 dB at 4 minutes into the test. From Figure 54, it can be seen that the maximum actuator voltage at 4 minutes is under 7.5 Vp. This is equivalent to 50% of available maximum power, or about 7 watts, on the most utilized actuator. The other actuators are operating well below this level. If the system were to be optimized using flight transfer functions, lower power levels may be possible. These low power levels might enable a lighter, less expensive actuator, making the whole noise control system cheaper.

Conclusions

Active Structural Acoustic Control (ASAC) been shown to be an effective aircraft interior noise control method. The ASAC system achieved good control of the blade passage frequency at low power. However, the ASAC system did not meet performance expectations, especially at higher harmonics. This has been shown both analytically and experimentally to be caused by changes in the dynamics of the structural acoustics of the aircraft brought about by cabin pressurization.

The PC-LMS control algorithm has been demonstrated to achieve significant noise reduction. The ability to individually adjust the control effort penalty and convergence rate of each orthogonal virtual control channel provides a means to increase both the stability and performance of the control system. The principal component domain transformation has also been shown to be a diagnostic tool useful during actuator location optimization and post processing analysis of the control system.

The locations for the actuators were optimized using a goal-directed combinatorial search. The method coupled actuator force constraints and coherence limits to produce a realistic prediction of a candidate system's noise reduction. The noise reduction predictions were computed using actuator transfer functions acquired during unpressurized ground tests. The use of the unpressurized transfer functions is shown to bias the optimization, reducing the effectiveness of the control system when the cabin is pressurized at cruise altitudes.

It is finally concluded that if an ASAC system is to reach full potential, then the transfer functions used in the controller and during actuator location optimization, must reflect in-flight, pressurized conditions.

References

1. C. R. Fuller. Apparatus and method for global noise reduction, 1987. U. S. Patent No. 4715599.

2. C. R. Fuller and J. D. Jones. Experiments on reduction of propeller induced interior noise by active control of cylinder vibration. *Journal of Sound and Vibration*, 112:389–395, 1987.

3. Harold C. Lester and Sylvie Lefebvre. Piezoelectric actuator models for active sound and vibration control of cylinders. *Journal of Intelligent Material Systems and Structures*, 4:295–306, July 1993.

4. S. D. Snyder and C. H. Hansen. Mechanisms of active noise control by vibration sources. *Journal of Sound and Vibration*, 147(3):519–525, 1991.

5. Richard J. Silcox, Sylvie Lefebvre, Vern L. Metcalf, Todd B. Beyer, and Chris R. Fuller. Evaluation of piezoceramic actuators for control of aircraft interior noise. In *DGLR/AIAA 14th Aeroacoustics Conference, Aachen, Germany, May 1992*, number AIAA 92-02-091, pages 542–551, 1992.

6. D. R. Thomas, P. A. Nelson, and S. J. Elliott. Active control of the transmission of sound through a thin cylindrical shell, part II: The minimization of acoustic potential energy. *Journal of Sound and Vibration*, 167(1):113–128, 1993.

7. P. A. Nelson and S. J. Elliott. *Active Control of Sound*. Academic Press, 1992.

8. S. J. Elliott, P. A. Nelson, I. M. Stothers, and C. C. Boucher. In-flight experiments on the active control of propeller-induced cabin noise. *Journal of Sound and Vibration*, 140(2):219–238, 1990.

9. J. C. Burgess. Active adaptive sound control in a duct: A computer simulation. *Journal of the Acoustical Society of America*, 70(3):715–726, September 1981.

10. Dennis R. Morgan. An analysis of multiple correlation cancellation loops with a filter in the auxiliary path. *IEEE Transactions on Acoustics, Speech, and Signal Processing*, ASSP-28(4):454–467, 1980.

11. Bernard Widrow and Samuel D. Stearns. *Adaptive Signal Processing*. Prentice-Hall, 1985.

12. Stephen J. Elliott, Ian M. Stothers, and Philip A. Nelson. A multiple error lms algorithm and its application to the active control of sound and vibration. *IEEE Transactions on Acoustics, Speech, and Signal Processing*, ASSP-35(10):1423–1434, October 1987.

13. Randolph H. Cabell. *A Principal Component Algorithm for Feedforward Active Noise and Vibration Control*. PhD thesis, Virginia Tech, Blacksburg, VA 24061, May 1998.

14. F. Glover. Tabu search: A tutorial. *Interfaces*, 20:74–94, 1990.

15. D. L. Palumbo and S. L. Padula. Optimization of an actuator array for the control of multifrequency noise in aircraft interiors. In *3rd AIAA/CEAS Aeroacoustics Conference, Atlanta, May 12–14, 1997*, number AIAA 97-1615, May 1997.

16. S. D. Snyder and C. H. Hansen. Using multiple regression to optimize active noise control system design. *Journal of Sound and Vibration*, 148(3):537–542, 1991.

17. Stephen J. Elliott, Christopher C. Boucher, and Philip A. Nelson. The behavior of a multiple channel active control system. *IEEE Transactions on Signal Processing*, 40(5):1041–1052, May 1992.

18. D. J. Rossetti, M. R. Jolly, and S. C. Southward. Control effort weighting in feedforward adaptive control systems. *Journal of the Acoustical Society of America*, 99(5):2955–2964, May 1996.

19. R. H. Cabell, H. C. Lester, and R. J. Silcox. The optimization of force inputs for active structural acoustic control using a neural network. Technical Report 107627, NASA, June 1992.

20. Robert L. Clark and Chris R. Fuller. Optimal placement of piezoelectric actuators and polyvinylidene fluoride error sensors in active structural acoustic control approaches. *Journal of the Acoustical Society of America*, 92(3):1521–1533, September 1992.

21. K. A. Cunefare and G. H. Koopmann. A boundary element approach to optimization of active noise control sources on three dimensional structures. *Journal of Vibration and Acoustics*, 113:387–394, July 1991.

22. G. P. Gibbs, S. Paxton, and C. R. Fuller. An experimental based actuator optimization scheme for active structural acoustic control of interior noise in aircraft. In *Proceedings of the Fifth Pan American Congress of Applied Mechanics, San Juan, Puerto Rico*, pages 407–411, January 1997.

23. Hareo Hamada, Noriyuki Takashima, and P. A. Nelson. Genetic algorithms used for active control of sound: Search and identification of noise sources. In *Active 95, Newport Beach, CA, July 6-9, 1995*, pages 33–38, Newport Beach, July 1995.

24. B. Nayroles, G. Touzot, and P. Villon. Using the diffuse approximation for optimizing the location of anti-sound sources. *Journal of Sound and Vibration*, 171(1):1–21, 1994.

25. Héctor M. Rodriguez, Ricardo A. Burdisso, and Chris R. Fuller. Optimum design for feedforward active structural acoustic control of complex structures. In *Active 95, Newport Beach, CA, July 6-9, 1995*, pages 335–346, Newport Beach, July 1995.

26. C. E. Ruckman and C. R. Fuller. Optimizing actuator locations in feedforward active control systems using subset selection. In *Second Conference on Recent Advances in Active Control of Sound and Vibration*, pages S122–S133, Blacksburg, Virginia, April 1993.

27. D. L. Palumbo, S. L. Padula, K. H. Lyle, J. H. Cline, and R. H. Cabell. Performance of optimized actuator and sensor arrays in an active noise control system. In *2nd AIAA/CEAS Aeroacoustics Conference (17th Aeroacoustics Conference), State College, PA, May 6–8, 1996*, number AIAA 96-1724, May 1996.

28. Bernard Widrow, John R. Glover Jr., John M. McCool, John Kaunitz, Charles S. Williams, Robert H. Hearn, James R. Zeidler, Eugene Dong Jr., and Robert C. Goodlin. Adaptive noise cancelling: Principles and applications. *Proceedings of the IEEE*, 63(12):1692–1716, December 1975.

29. C. F. Ross. *Active Control of Sound*. PhD thesis, University of Cambridge, Cambridge, England, 1980.

30. Jason Caton. *FIX ME: UNKNOWN MASTERS THESIS*. PhD thesis, George Washington University JIAFS, Hampton, VA 23681, May 1998.

31. F. W. Grosveld and T. B. Beyer. Modal characteristics of a stiffened composite cylinder with open and closed end conditions. In *AIAA 10th Aeroacoustics Conference, Seattle, WA, July 9–11, 1986*, number AIAA 86-1908. AIAA, July 1986.

32. Earl G. Williams, Brian H. Houston, and Joseph A. Bucaro. Broadband nearfield acoustical holography for vibrating cylinders. *Journal of the Acoustical Society of America*, 86(2):674–9, 1989.

33. Julius S. Bendat and Allan G. Piersol. *Random Data*. Wiley-Interscience, New York, second edition, 1986.

34. C.F. Ross and M.R.J. Purver. Active cabin noise control. *Active 97, Budapest Hungary, 1997*. pages 39-56, 1997.

35. C.M. Dorling, G.P. Eatwell, S.M. Hutchins, C.F. Ross and S.G.C. Sutcliff. A demonstration of active noise reduction in an aircraft cabin. *Journal of Sound and Vibration*, 128(1):358-360, 1989.

36. S. J. Elliott, P. A. Nelson, I. M. Stothers and C. C. Boucher. In-flight experiments on the active control of propeller-induced cabin noise. *Journal of Sound and Vibration*, 140(2):219-238, 1990

37. S. J. Elliott, P. A. Nelson, I. M. Stothers, and C. C. Boucher. Preliminary results of in-flight experiments on the active control of propeller-induced cabin noise. *Journal of Sound and Vibration*. 128(2):355-357, 1989.

Tables

Table I. Components of Tabu Search Algorithm

Component	Description
Cost Function	Predicted Noise Reduction
Candidate Pool	Database of Possible Actuator Locations
N_a	Number of Elements in Pool
N_c	Number of Elements in Desired Array
N_i	Number of Iterations in Search
State	A Subset of the Pool of Size, N_c
State Space	Set of All Possible States (Subsets)
Current State	Present Location of Search
Best State	State with Lowest Cost Function
Move Function	Swap 1 Element of Subset with 1 from Pool
Neighborhood	All States 1 *Move* away from Current State
Tabu List	List of All Previously Visited States

Table II . FEA Noise Control Predictions

Condition	104 Hz ΔdB	208 Hz ΔdB	312 Hz ΔdB	416 Hz ΔdB	520 Hz ΔdB
Ground	-17.9	-2.6	-1.8	-3.6	-4.1
In-Flight	-13.1	No Control			

Table III. Actuator Locations

Actuator Number	Frame	Bay	12 Actuator
1	1	15	x
2	1	20	x
3	2	1	x
4	2	4	x
5	2	11	
6	2	17	x
7	3	14	x
8	3	17	x
9	4	4	x
10	5	4	x
11	5	17	
12	6	4	x
13	7	11	x
14	9	4	
15	9	15	
16	9	17	x
17	10	11	
18	13	17	
19	14	4	
20	15	17	
21	16	4	

Table IV. Predicted Noise Reduction for 21 Actuator Configuration

Weighting	Overall, dB	1st Harmonic, dB	2nd Harmonic, dB	3rd Harmonic, dB
Linear	-12.9	-13.5	-8.6	-6.3
A-weight	-10.8	-13.5	-8.7	-6.4

Table V. Raytheon 1900D Specifications

PERFORMANCE	**U.S.**	***METRIC***
Max Cruise Speed	288 kt	533 kph
Certified Ceiling	25,000 ft	7,620 m
Max Range	1,575 nm	2,919 km

ENGINES: Pratt & Whitney		
PT6A-67D	1,279 shp	

WEIGHTS	**U.S.**	**METRIC**
Basic Operating Weight	10,615 lb	4,815 kg
Useful Load	6,445 lb	2,923 kg

DIMENSIONS(External)	**U.S.**	**METRIC**
Wingspan	57.9 ft	17.7 m
Max Airplane length	57.8 ft	17.6 m
Max Tail Height	14.9 ft	4.6 m

DIMENSIONS(Internal)	**U.S.**	***METRIC***
Length	407 in	1,034 cm
Width	54 in	137 cm
Height	71 in	180 cm

Table VI. Coherence of Primary Field

Frequency, Hz	Coherence	Noise Reduction
103	0.988	19.1
206	0.934	11.8
309	0.861	8.6
412	0.859	8.5
515	0.827	7.6

Table VII. Equipment List

Item	Number
Controller	
Rack-mount PC	1
DSP Board	1
I/O Board	3; 48 in; 24 out
Tach Interface	1
Acquisition	
ICP Conditioners	3; 48 channels
Microphones	32
Accelerometers	12
Digital Tape	48 channels
Control	
Amplifiers	4; 24 channels
Actuators	24 pairs
Misc.	
Oscilloscope	1
Monitor	1
Keyboard	1
Mouse	1

Table VIII. Specifications of 130B10

Response	Free-field
Sensitivity	35mV/Pa
Frequency Range	20-7,000 Hz (± 1 dB)
Noise Floor	15 dB SPL
Linearity(<3%)	>128 dB SPL
Saturation Pt.	132 dB SPL
Directivity	Omnidirectional
Temp. Effects	-10 to 65° C < ± 0.5 dB

Table IX. Specs for IFX 15

Peak Force	75 N (17 lbf) @ 103 Hz
Power	12 W
Resistance	7.5 Ω (DC)
Resonant Freq.	95 Hz
Weight	245 gm (0.5 lb)
Dimensions	64x25x36 mm (2.5x1x1.4 in)

Table X. Test Points

Flight 1			Flight 2		
Run No.	Event	Time (min)	Run No.	Event	Time (min)
	System Identification	23		System Identification	28
1.1a	bpf	8	2.1a	bpf	7
1.2b	bpf, right engine	5	2.1b	1,2,3 bpf linear	6
1.3a	2bpf	7	2.3a	1,2,3 bpf A-weight	6
1.5a	3bpf	5	2.5a	1,2,3 bpf linear, 8x12 cfg	7
1.7a	bpf, 8x12 configuration	4	2.6a	2bpf	4
1.8a	bpf, 8x8 configuration	4	2.7a	1,2,3 bpf, descent	17
1.9a	bpf, descent	20			

Table XI. Condition Numbers Of Transfer Function Matrices

Harmonic	Ground	Flight 1	Flight 2
1	138.2	533.0	580.0
2	54	38.8	46.1
3	30	21.1	21.1

Table XII. Infinity Norms Of Transfer Function Matrices

Harmonic	Ground	Flight 1	Flight 2
1	15.4	6.48	5.80
2	3.7	1.92	1.81
3	2.4	1.18	1.16

Table XIII. Comparison of Predicted vs. Achieved Noise Reduction for Reduced, 8x12, Configuration

	Overall, ΔdB	1st Harmonic, ΔdB	2nd Harmonic, ΔdB	3rd Harmonic, ΔdB
Predicted	-9.9	-10.5	-6.0	-4.0
Achieved	-5.3	-6.1	-0.2	-1.6

Table XIV. Comparison of Predicted vs. Achieved Noise Reduction, 21 Actuators

Weighting	Overall, ΔdB	1st Harmonic, ΔdB	2nd Harmonic, ΔdB	3rd Harmonic, ΔdB
Predicted				
Linear	-12.9	-13.5	-8.6	-6.3
A-weight	-10.8	-13.5	-8.7	-6.4
Achieved				
Linear	-8.1	-10.2	-3.3	-1.6
A-weight	-4.4	-9.9	-2.3	-2.6

Figures

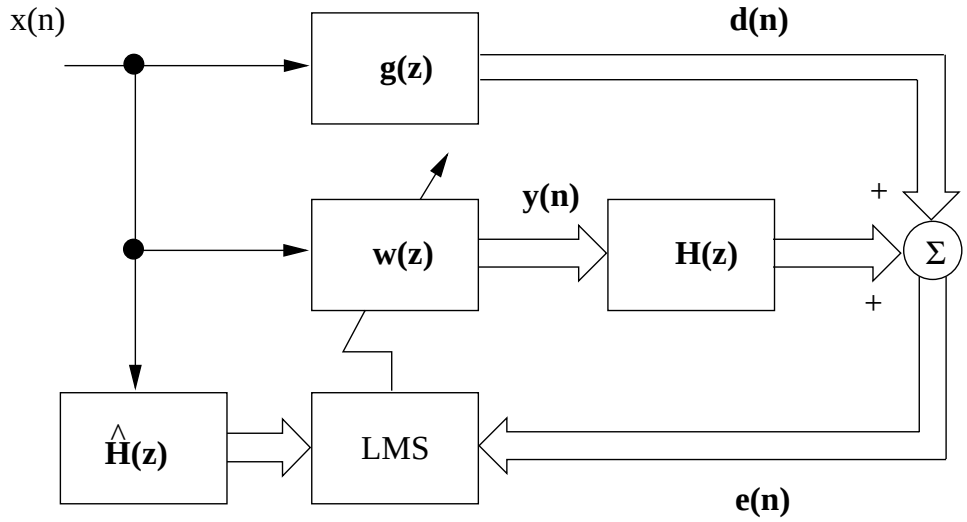

Figure 1. Multiple Error LMS Algorithm

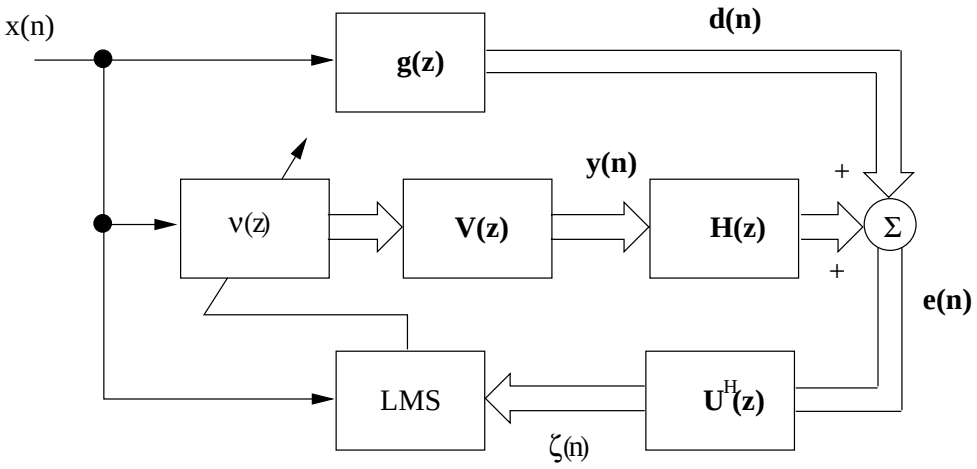

Figure 2. Principal Component LMS

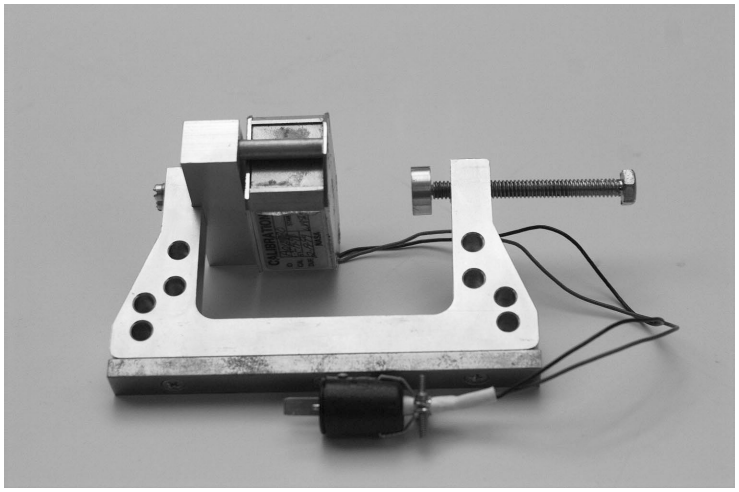

Figure 3. Actuator Mounted in Clamp

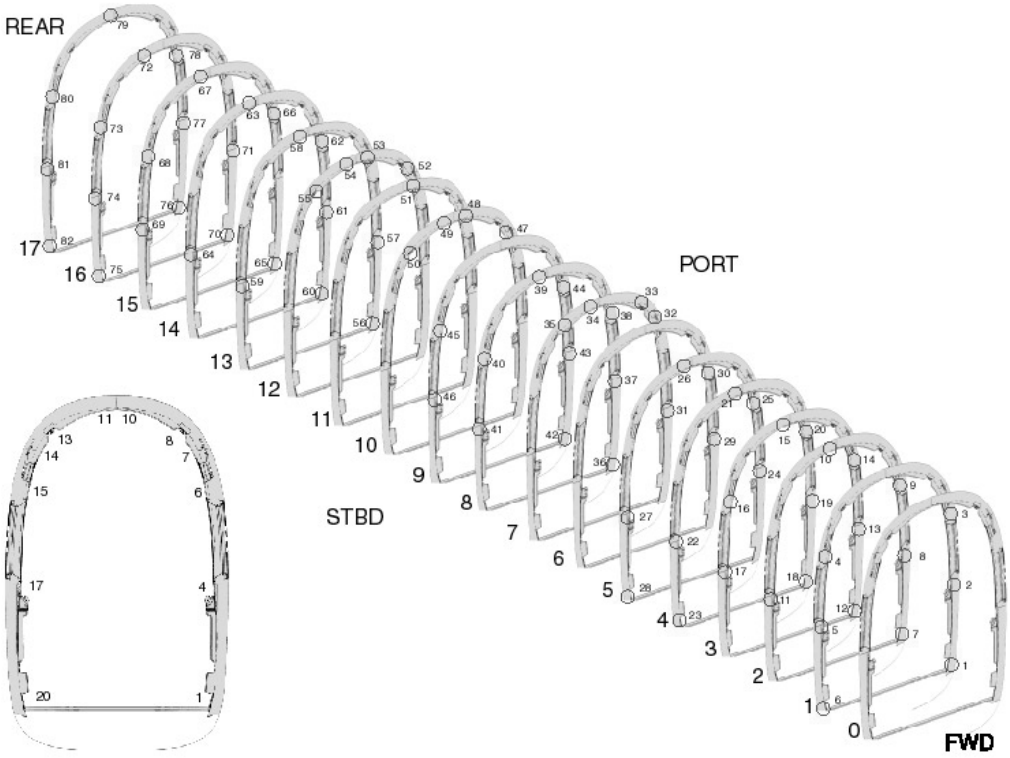

Figure 4. Actuator Locations Sampled on 1900D Frame

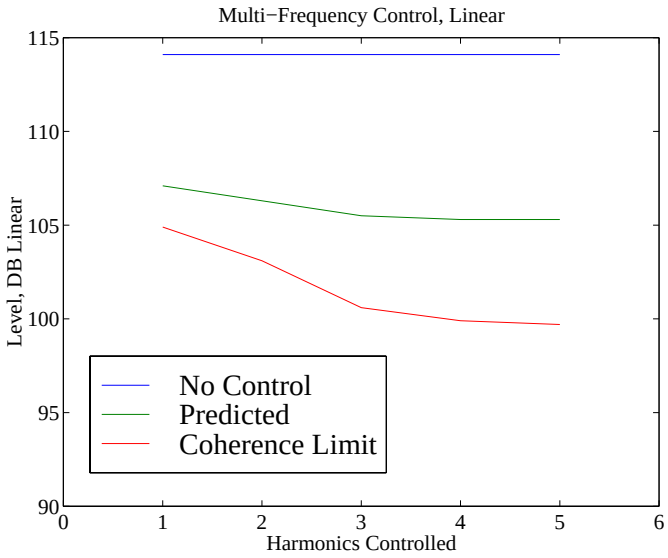

Figure 5. Total Noise Control, Linear

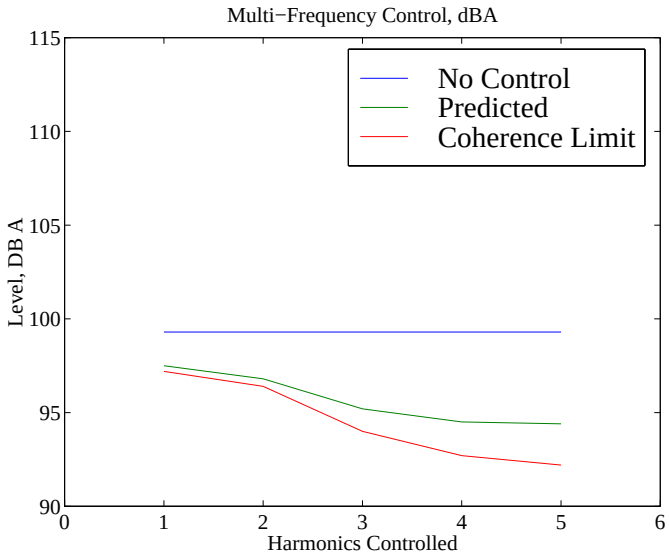

Figure 6. Total Noise Control, dBA

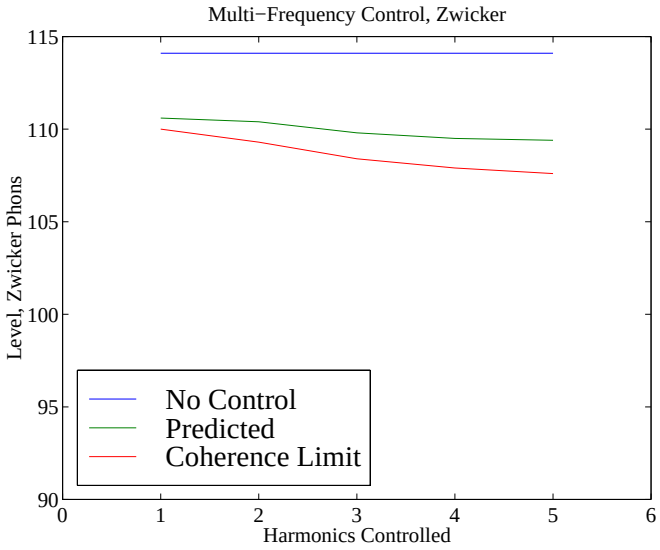

Figure 7. Total Noise Control, Zwicker

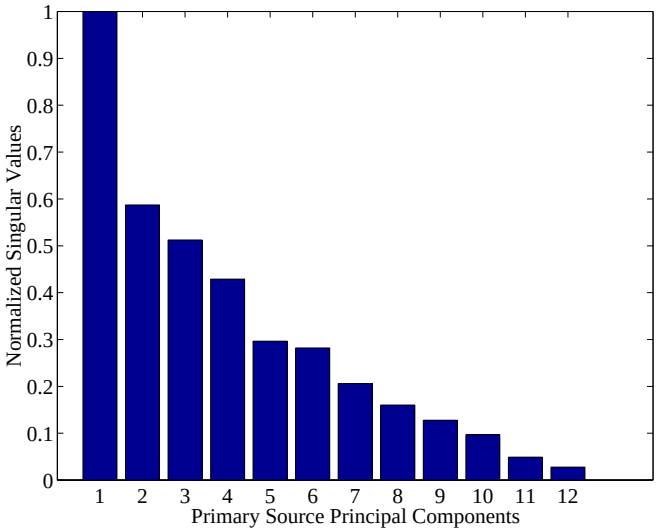

Figure 8. Typical Singular Values

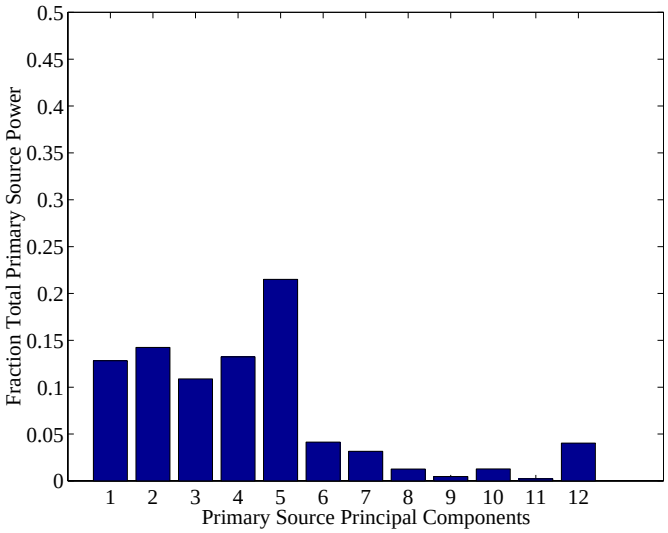

Figure 9. PCs Using a Random Actuator Set

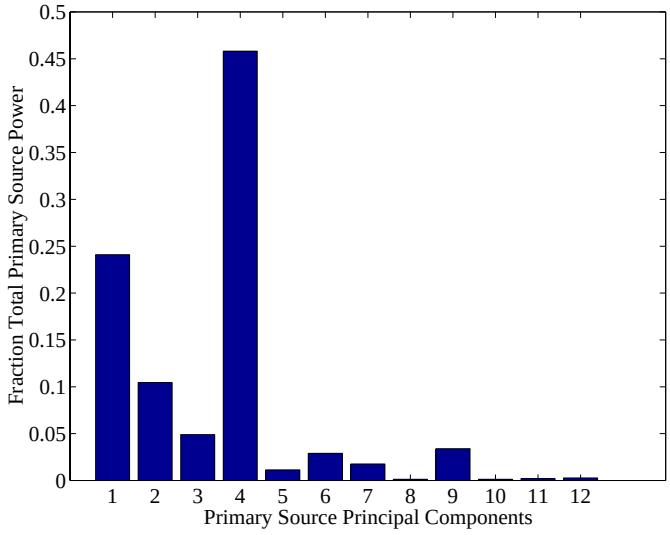

Figure 10. PCs optimized Using Nominal Constraints

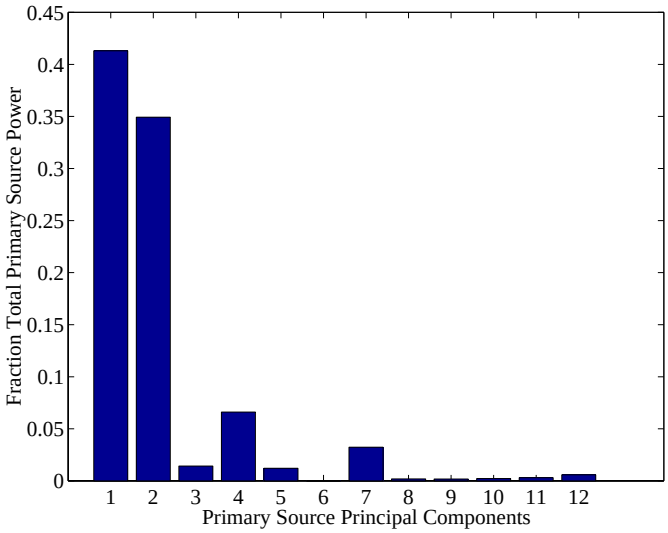

Figure 11. PCs Optimized Over Constrained

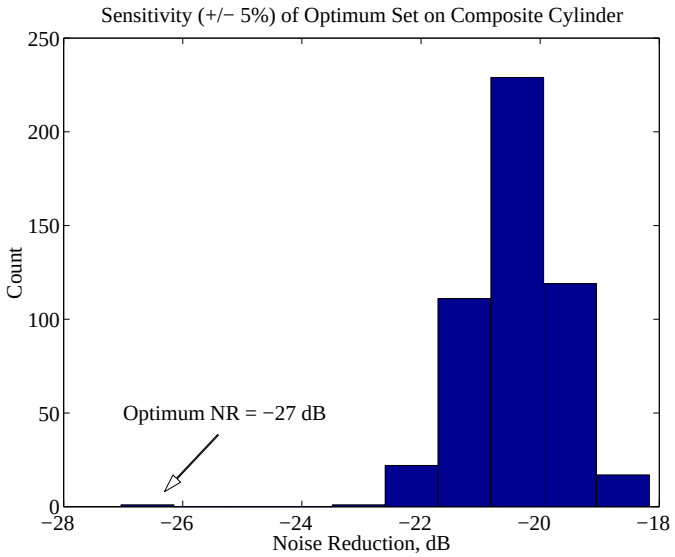

Figure 12. Sensitivity of Noise Reduction on Composite Cylinder

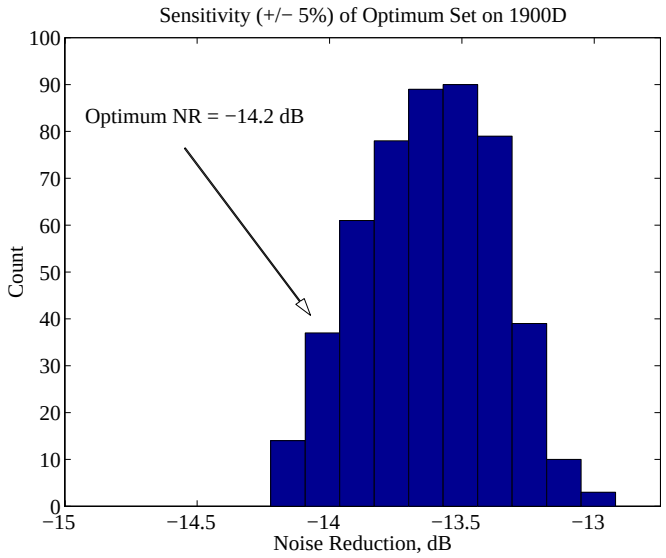

Figure 13. Sensitivity of Noise Reduction on 1900D

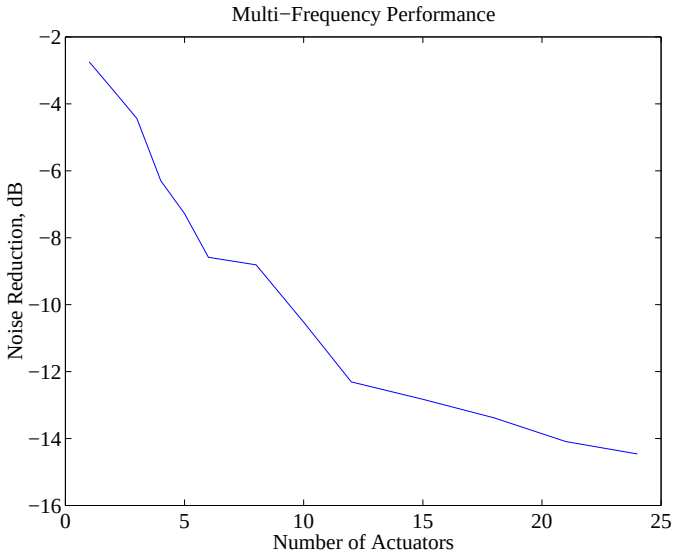

Figure 14. Noise Reduction vs. No. Of Actuators

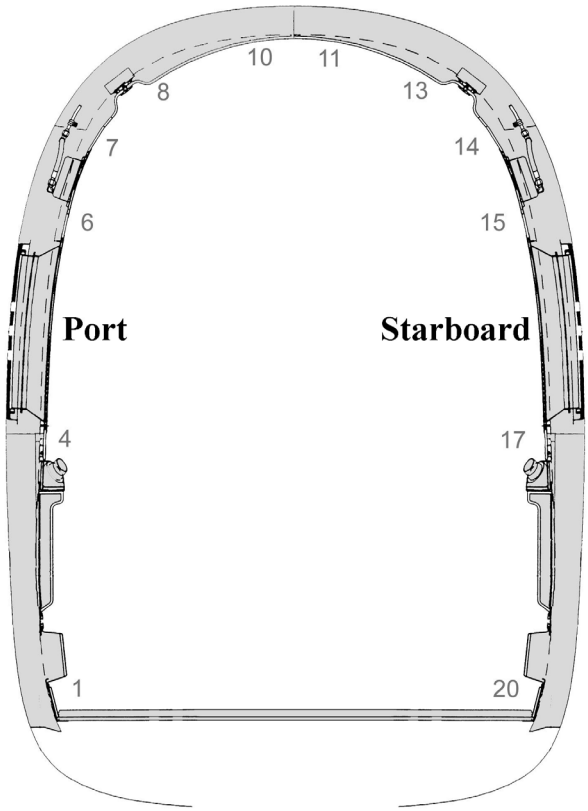

Figure 15 . Bay Locations on 1900D Frame

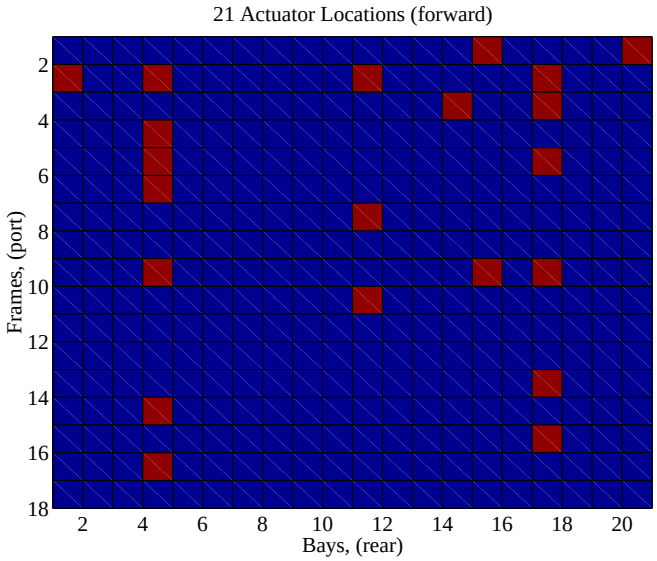

Figure 16. Actuator Mounting Locations on 1900D

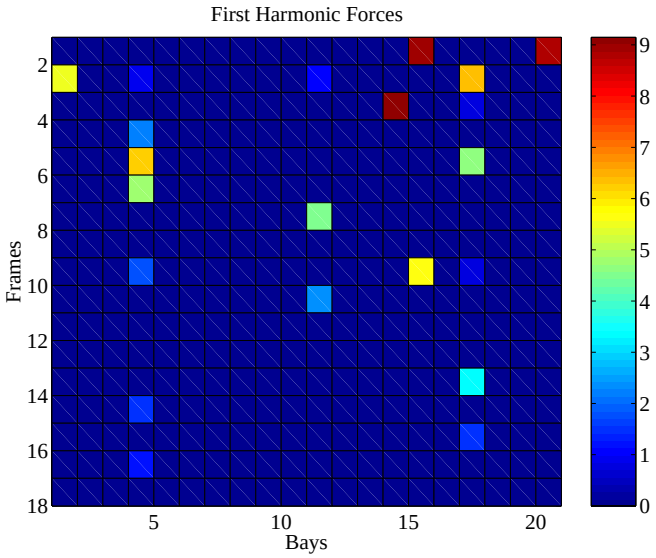

Figure 17. Actuator Forces, 1st Harmonic

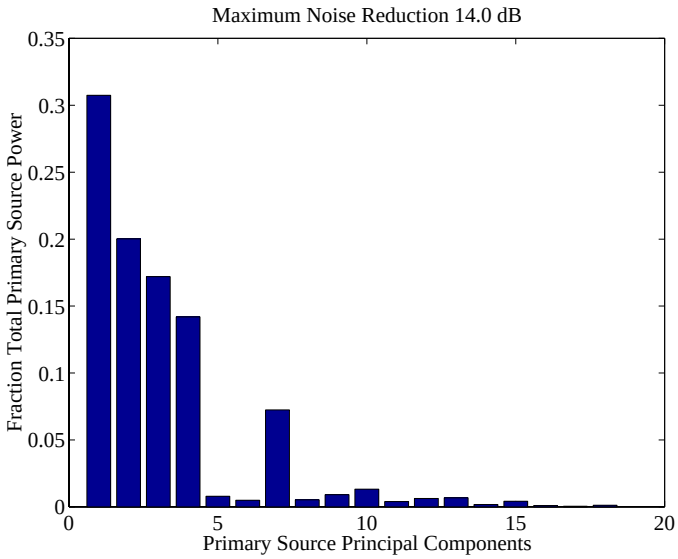

Figure 18. Primary PCs, 1st Harmonic

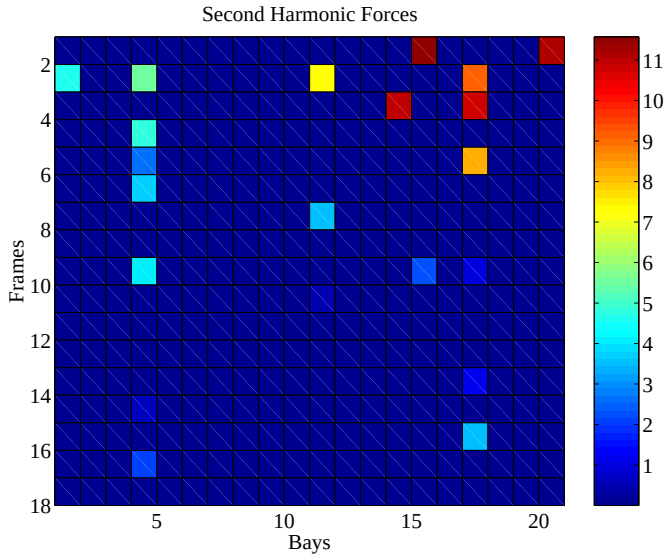

Figure 19. Actuator Forces, 2nd Harmonic

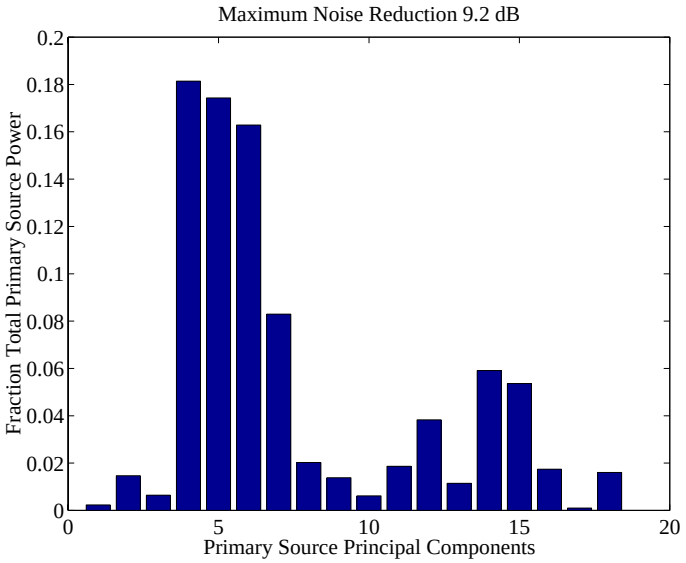

Figure 20. Primary PCs, 2nd Harmonic

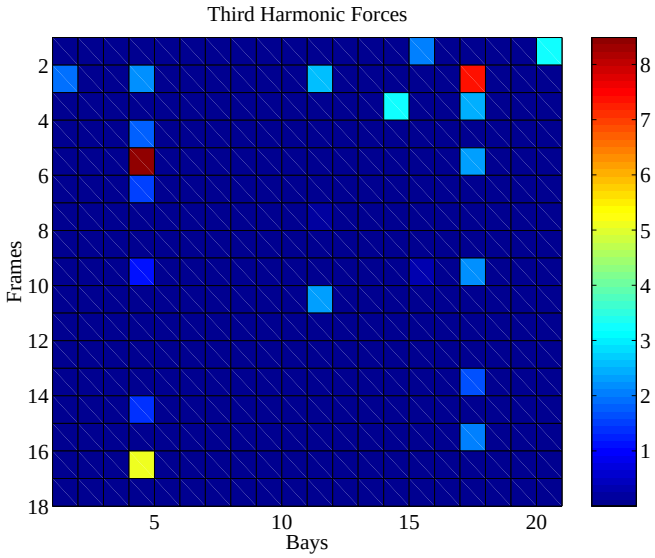

Figure 21. Actuator Forces, 3rd Harmonic

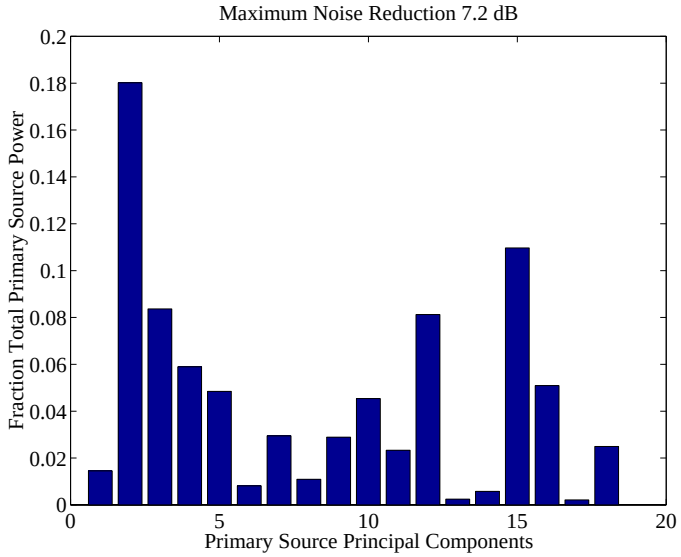

Figure 22. Primary PCs, 3rd Harmonic

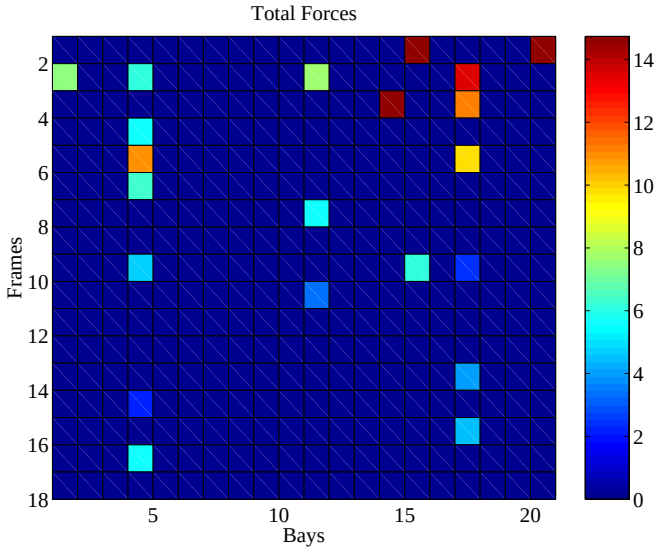

Figure 23. Total Forces on Actuators

Figure 24. Raytheon/Beech 1900D

Figure 25. 1900D Passenger Cabin

Figure 26. NRL Mic Rig in 1900D

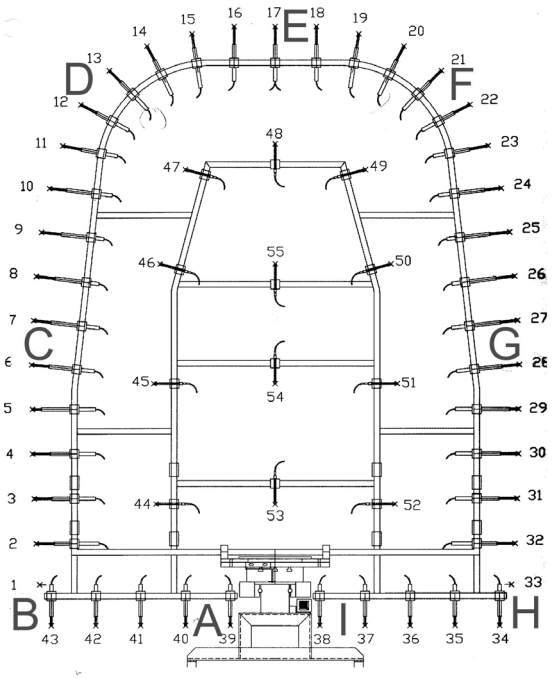

Figure 27. Mic Rig Detail Drawing

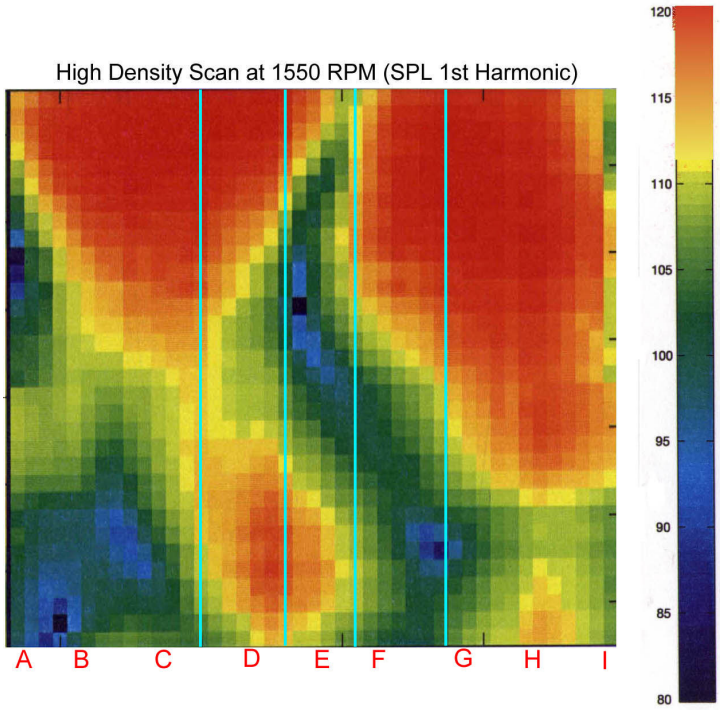

Figure 28. Pressure Map at 103 Hz.

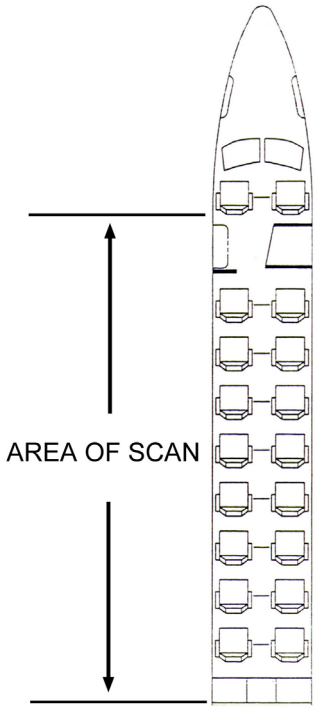

Figure 29. Sketch Showing Area of Scan

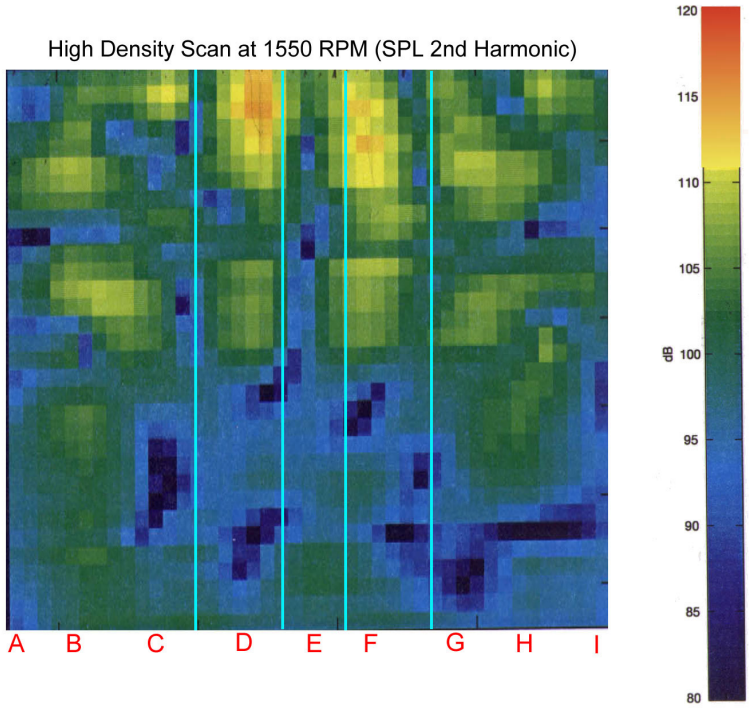

Figure 30. Pressure Map at 206 Hz

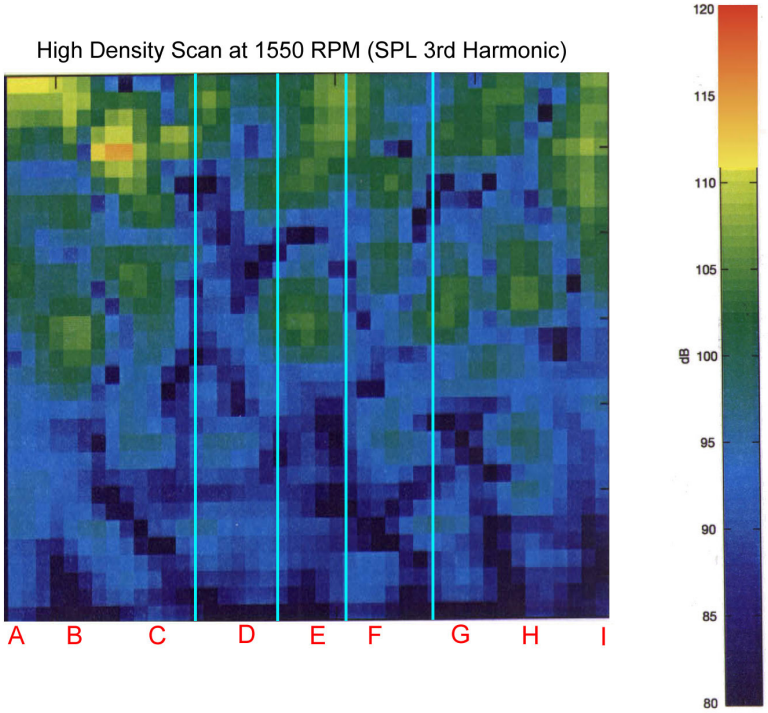

Figure 31. Pressure Map at 309 Hz

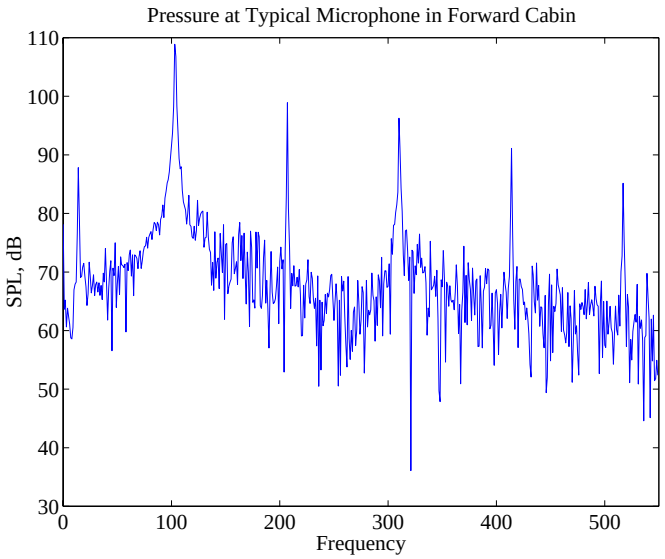

Figure 32. Spectrum of Typical Microphone

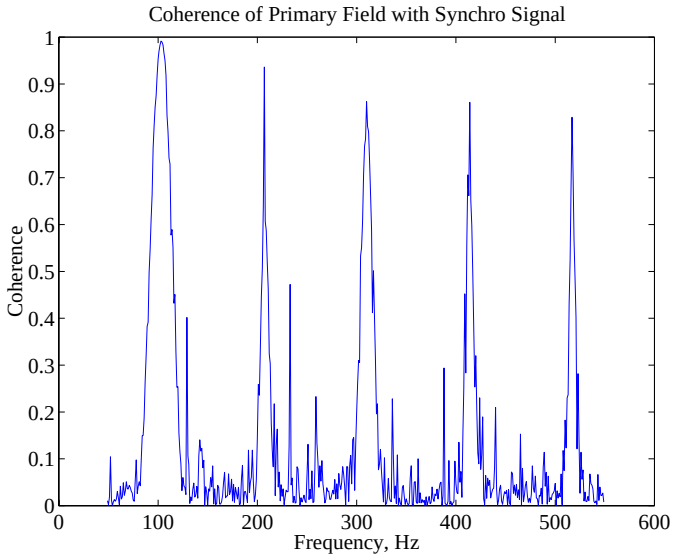

Figure 33. Coherence of Primary Field

ANC Block Diagram

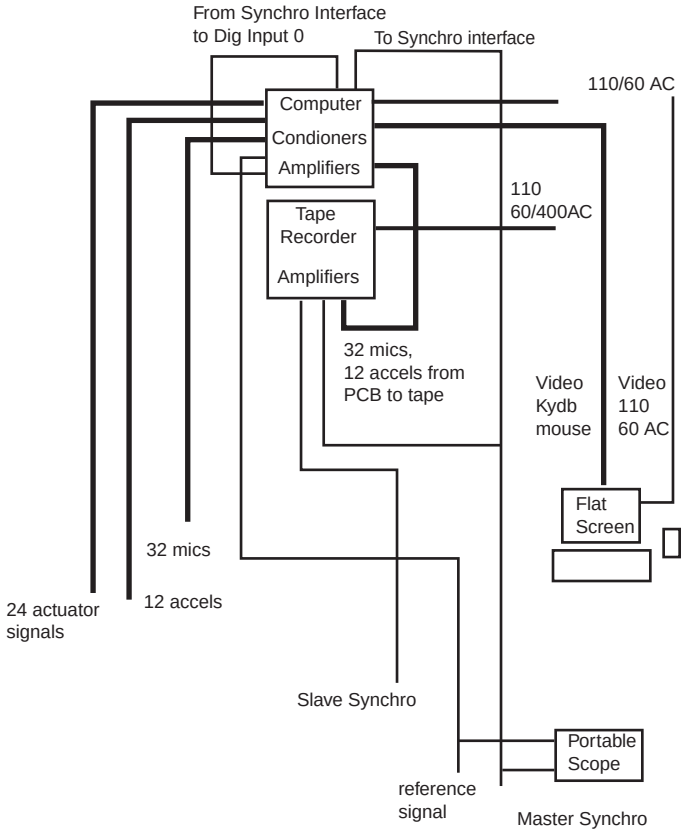

Figure 34. System Block Diagram

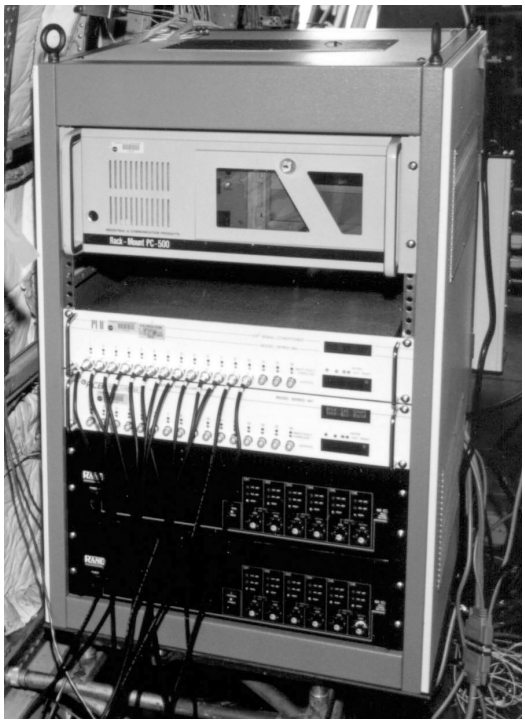

Figure 35. Controller Rack

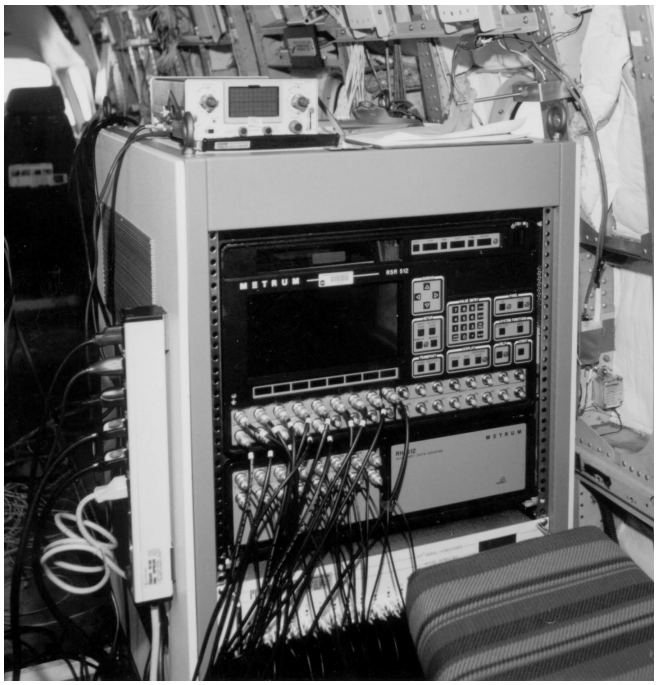

Figure 36. Tape Deck Rack

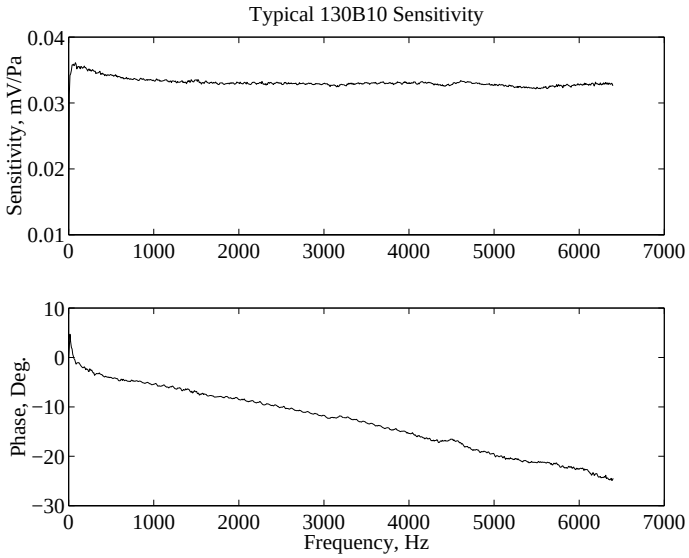

Figure 37. Sensitivity of 130B10

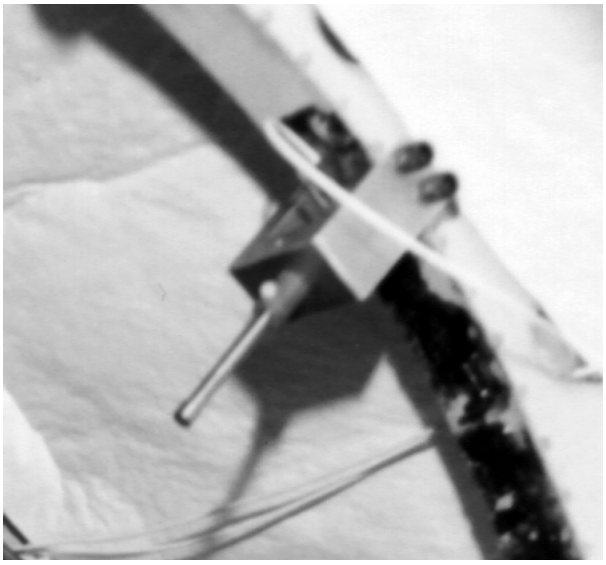

Figure 38. 130B10 Mounted on Frame

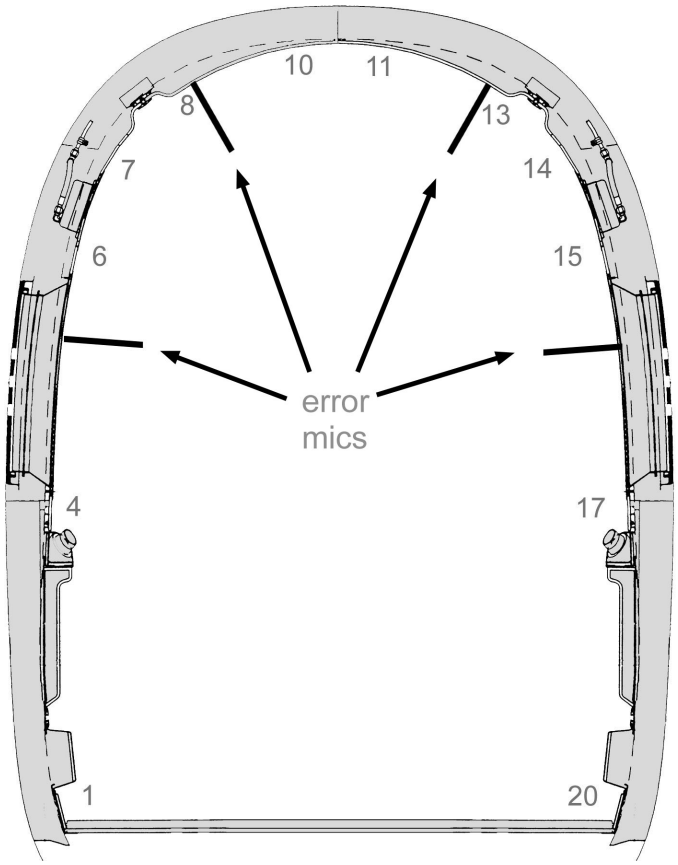

Figure 39. Microphone Locations

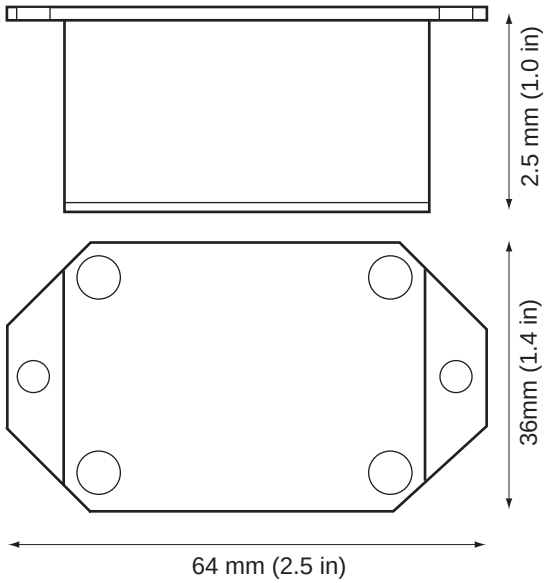

Figure 40. Sketch of IFX 15

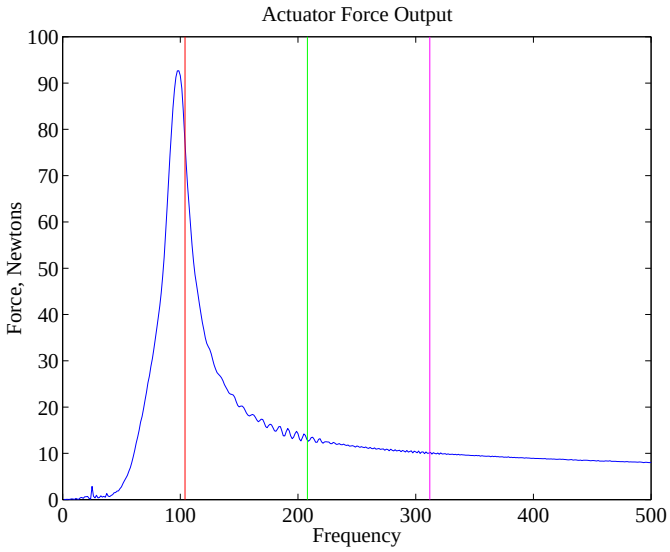

Figure 41. IFX 15 Magnitude Response

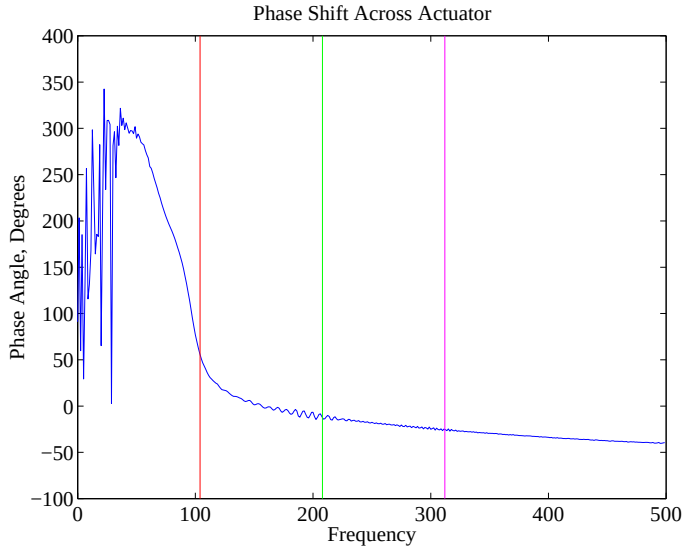

Figure 42. IFX 15 Phase Response

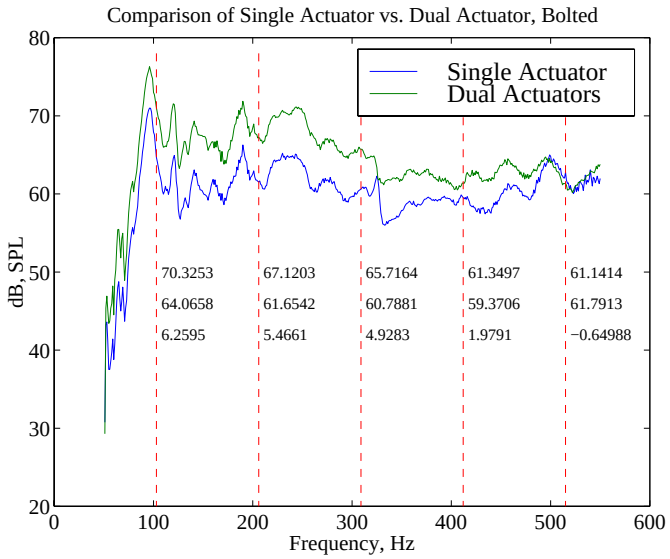

Figure 43. Single vs. Dual Actuators

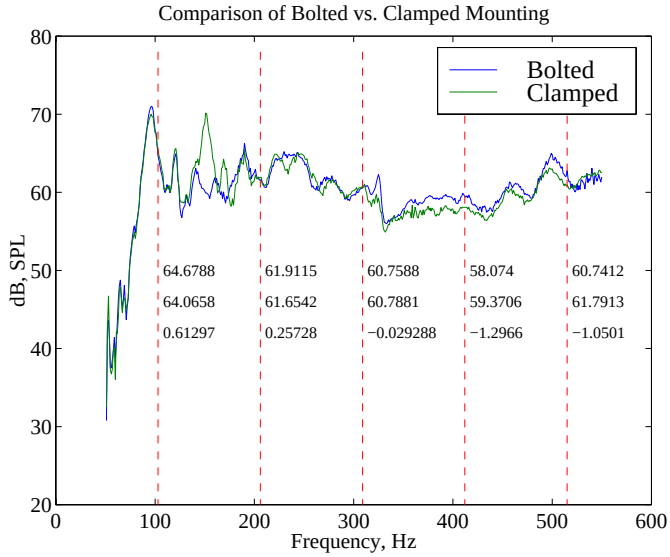

Figure 44. Bolted vs. Clamped Actuators

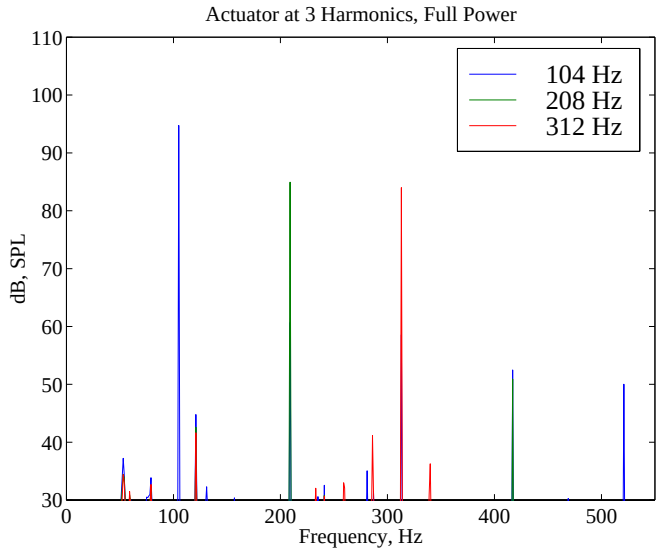

Figure 45. Full Power Output of Single Actuators Tuned to 95, 180 and 267 Hz

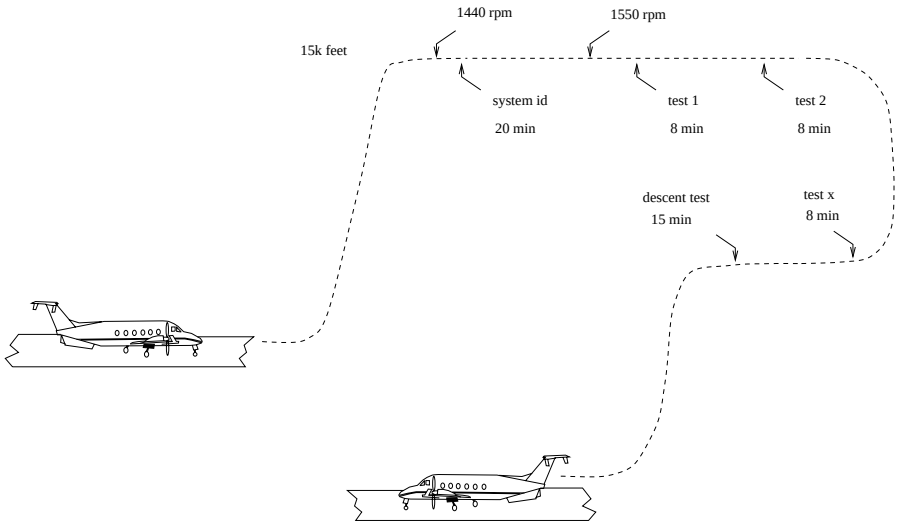

Figure 46. Flight Profile

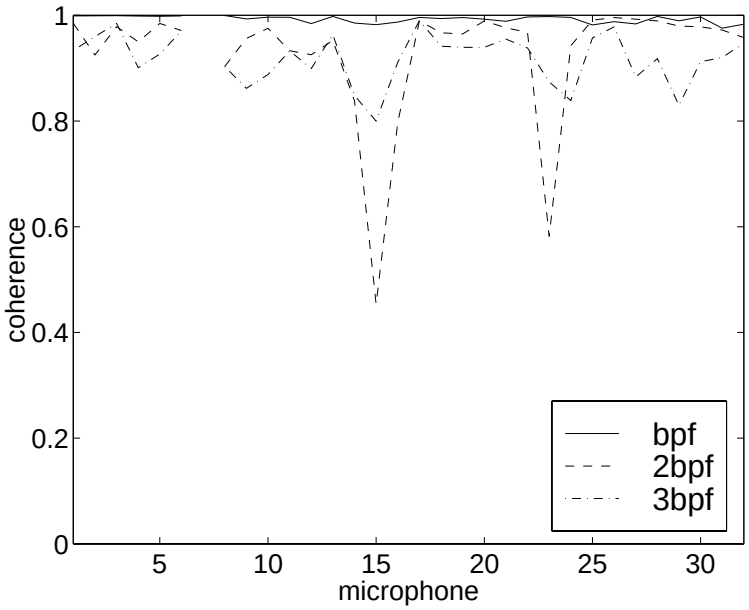

Figure 47. Reference to Primary Coherence, Flight 2, Run 5a

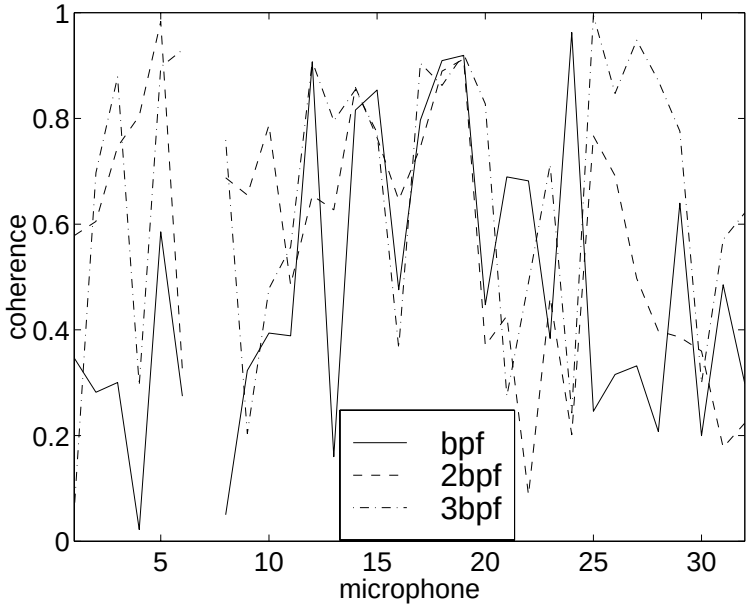

Figure 48. Reference to Primary Coherence, Flight 1, Run 2a

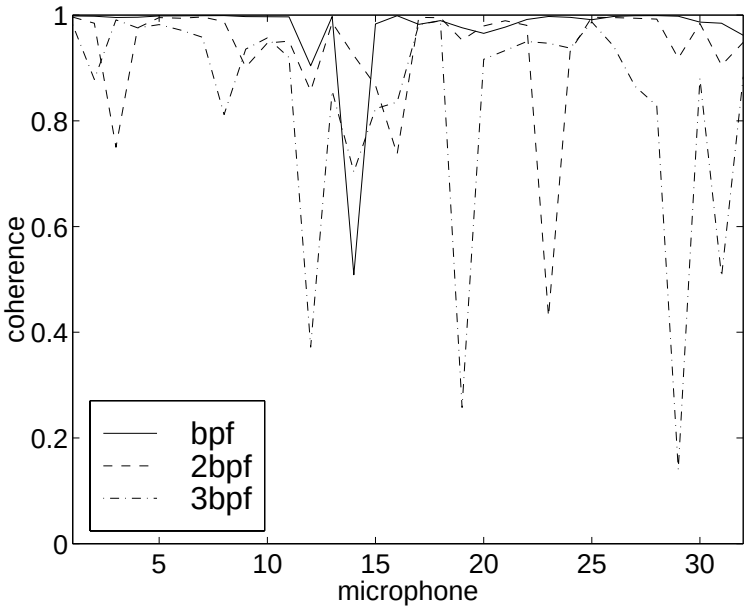

Figure 49. Reference to Primary Coherence, single engine

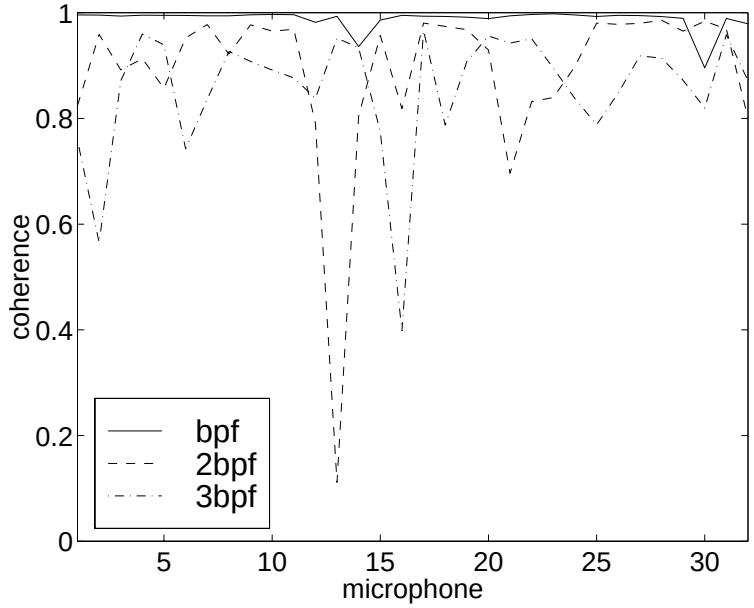

Figure 50. Reference to Primary Coherence, two engines

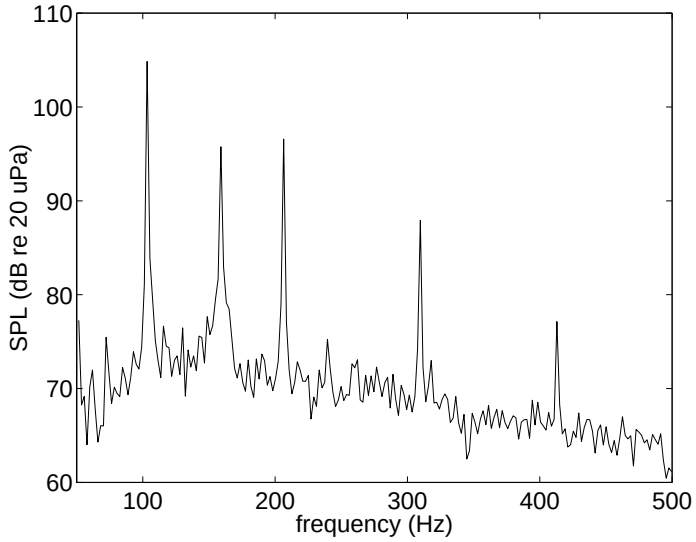

Figure 51. SPL before control, Flight 2, run 1a

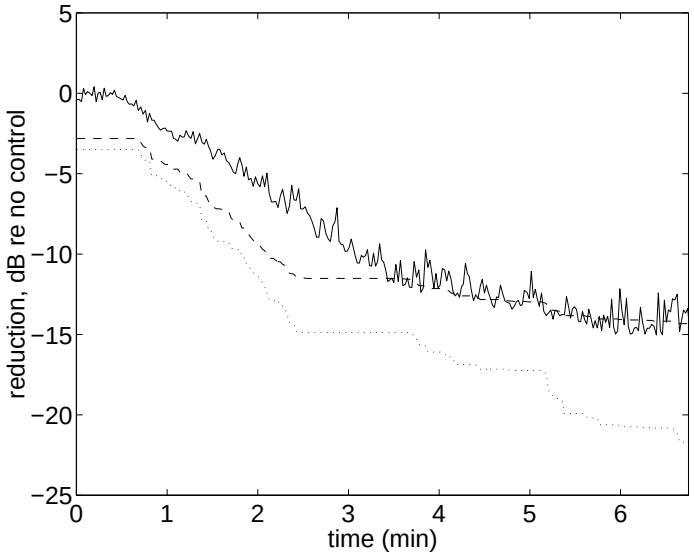

Figure 52. Reduction of bpf: - measured; -- predicted; ... predicted using unity coherence, Flight 2, run 1a

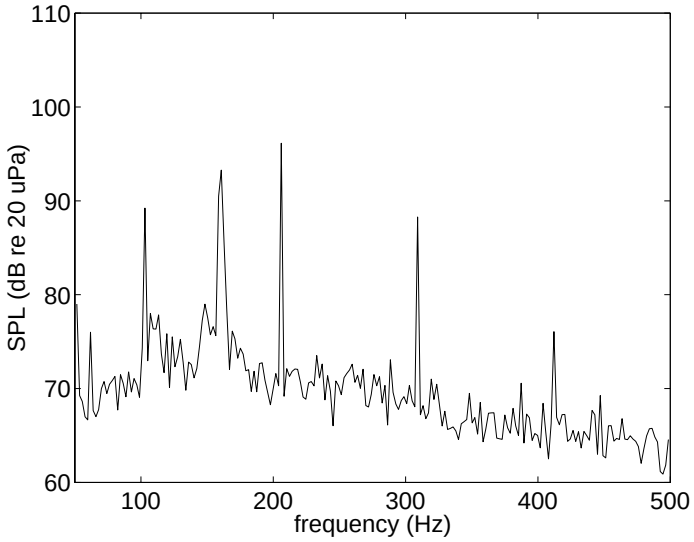

Figure 53. SPL after control, Flight 2, run 1a

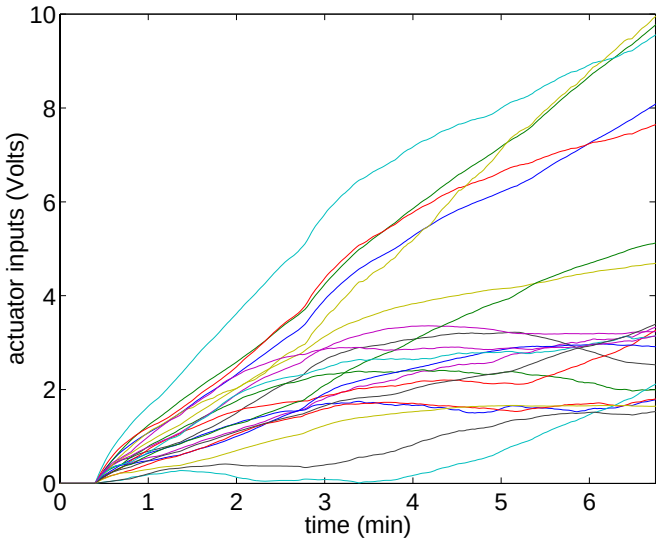

Figure 54. Actuator input voltages (Flight 2, run 1a)

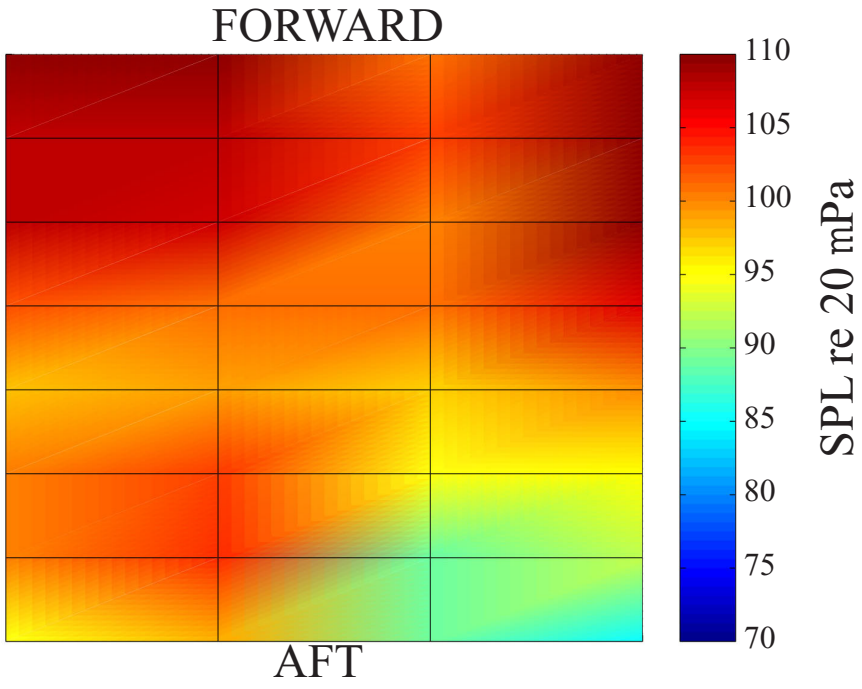

Figure 55. Microphone responses at bpf before control (Flight 2, run 1a)

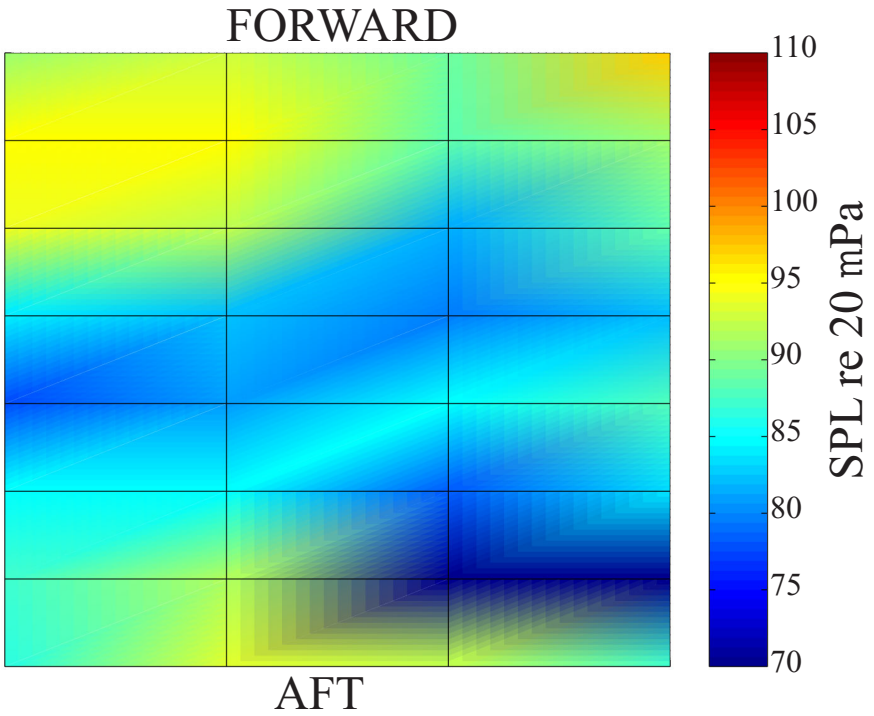

Figure 56. Microphone responses after control (Flight 2, run 1a)

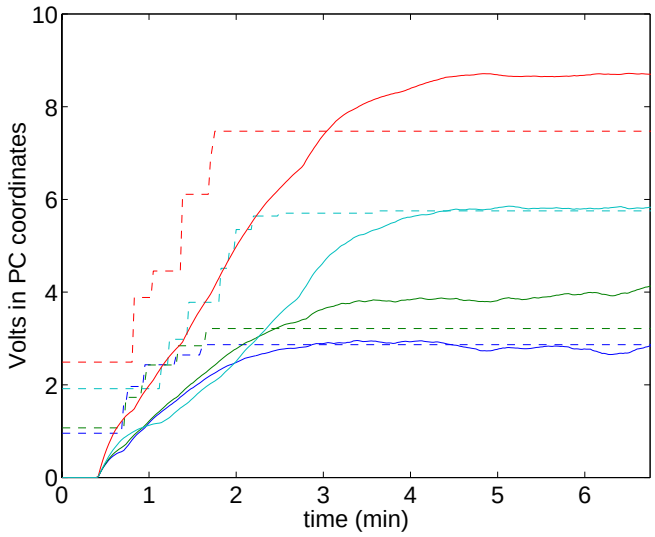

Figure 57. Principal Component Inputs (Flight 2, run 1a): - measured; -- predicted; blue<>PC1; green<>PC2; red<>PC3; light blue<>PC4

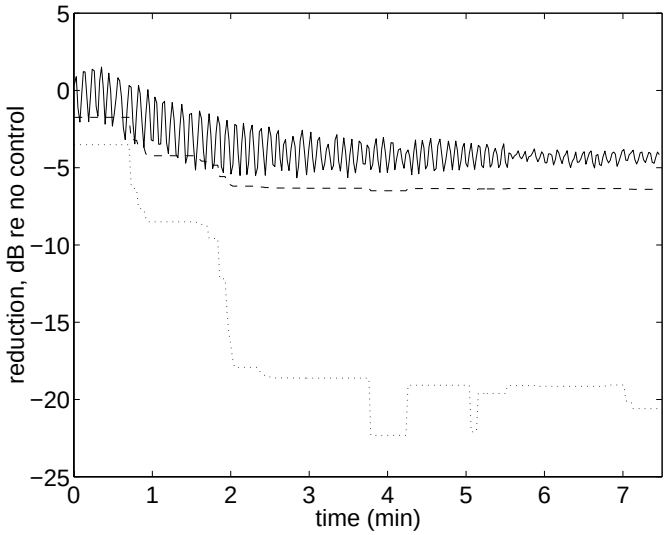

Figure 58. Reduction of 1st Harmonic (Flight 1, run 1a): - measured; --predicted; ...predicted with unity coherence

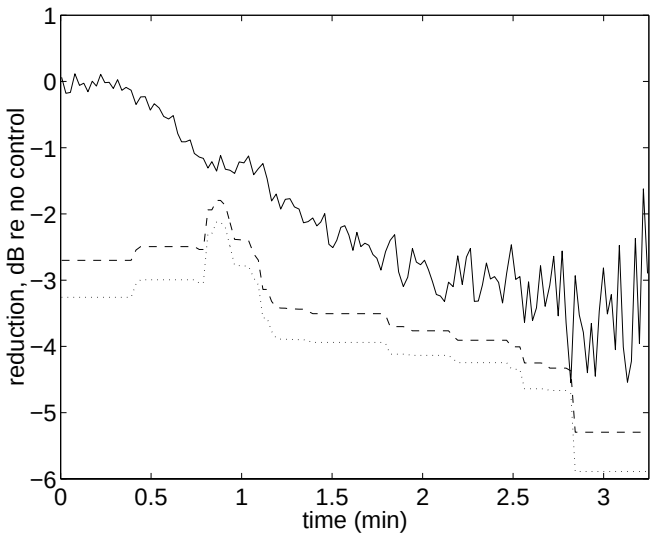

Figure 59. Reduction of 2nd Harmonic (Flight 2, run 6a): - measured; --predicted; ...predicted using unity coherence

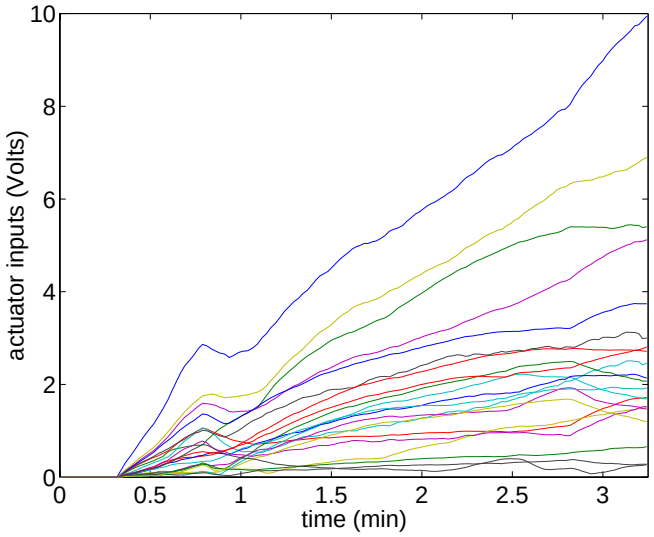

Figure 60. Actuator Input Voltage (Flight 2, run 6a)

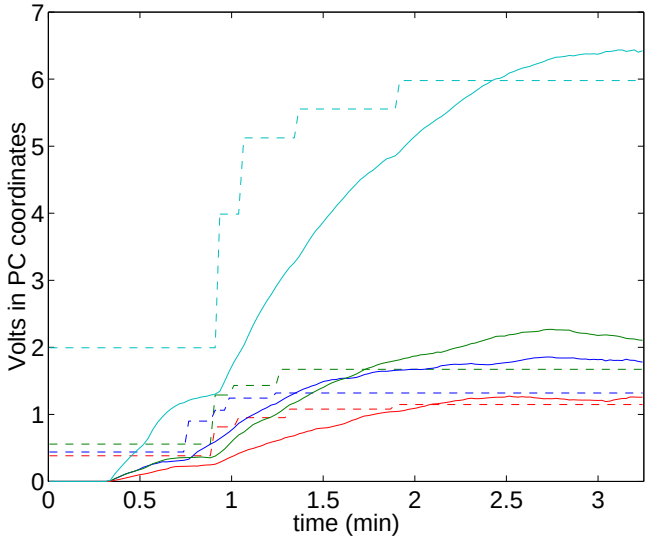

Figure 61. Prinicipal Component inputs (Flight 2, run 6a: - measured; --predicted; blue<>PC1; green<>PC2; red<>PC3; light blue<>PC4

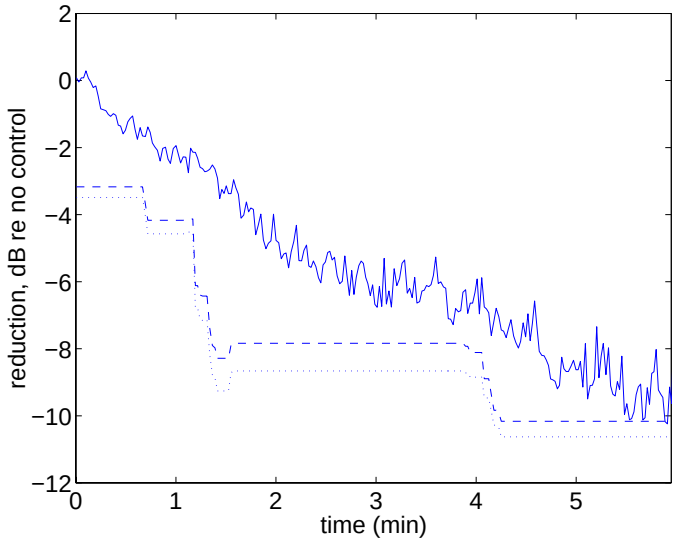

Figure 62. Reduction of 1st Harmonic (Flight 2, run 1b): - measured; --predicted; ...predicted using unity coherence

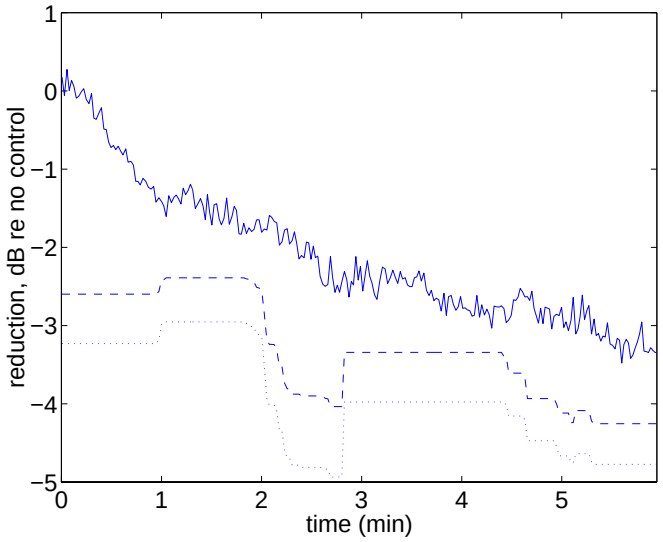

Figure 63. Reduction of 2nd Harmonic (Flight 2, run 1b): -measured; --predicted; ...predicted using unity coherence

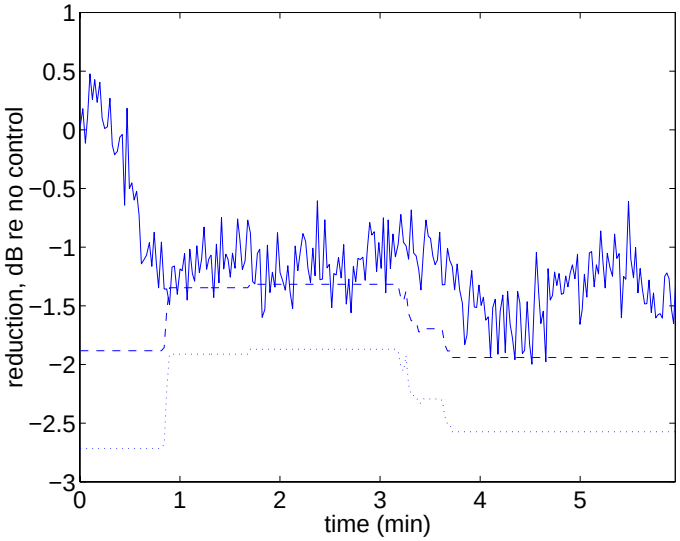

Figure 64. Reduction of 3rd Harmonic (Flight 2, run 1b): -measured; --predicted; ...predicted using unity coherence

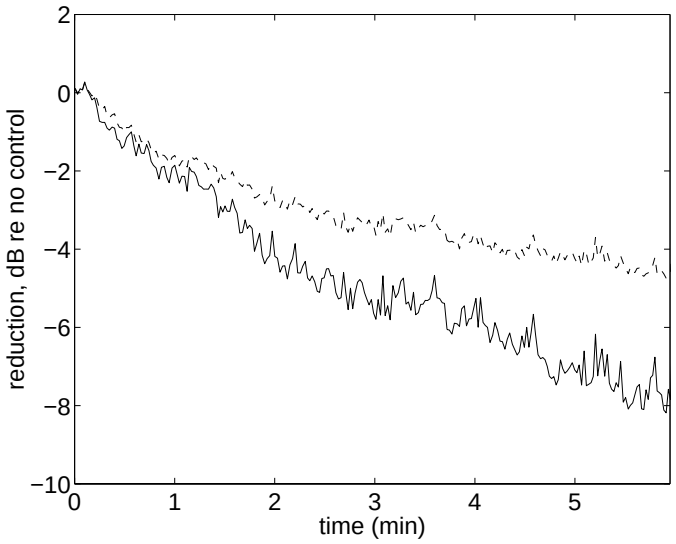

Figure 65. Reduction of cost function (Flight 2, run 1b): -linear; --A-weighted

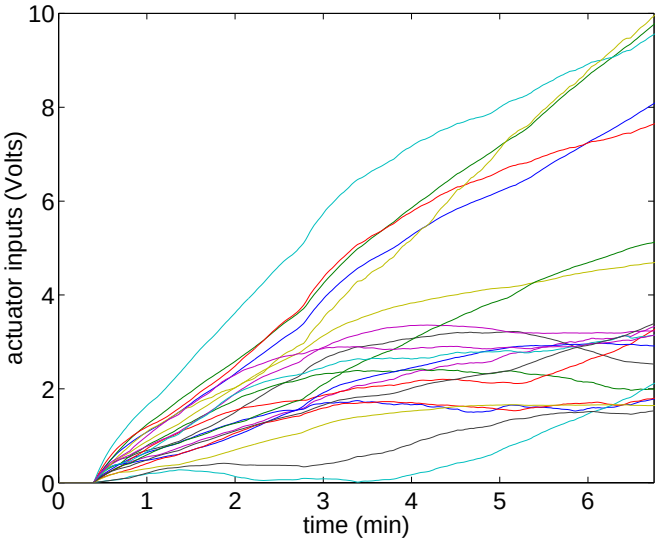

Figure 66. Actuator input voltages (Flight 2, run 1b)

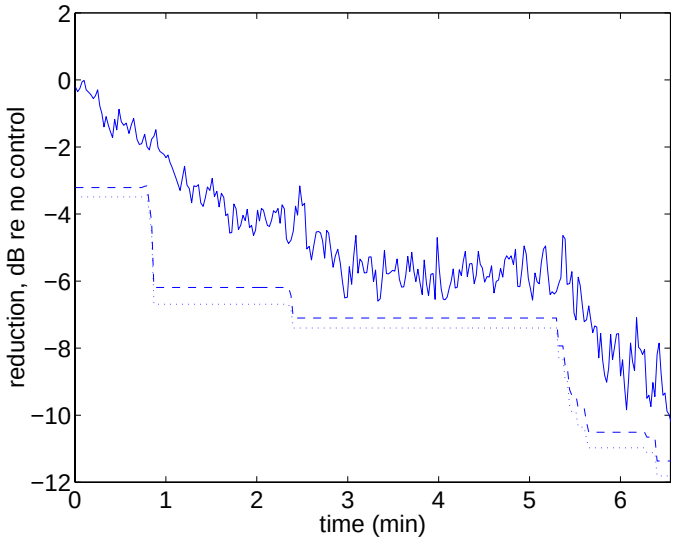

Figure 67. Reduction of 1st Harmonic (Flight 2, run 3a): - measured; --predicted; ...predicted using unity coherence

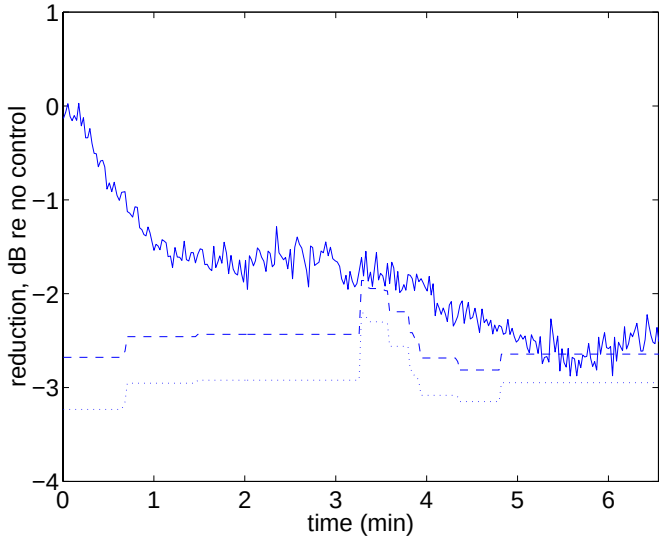

Figure 68. Reduction of 2nd Harmonic (Flight 2, run 6a): - measured; --predicted; ...predicted using unity coherence

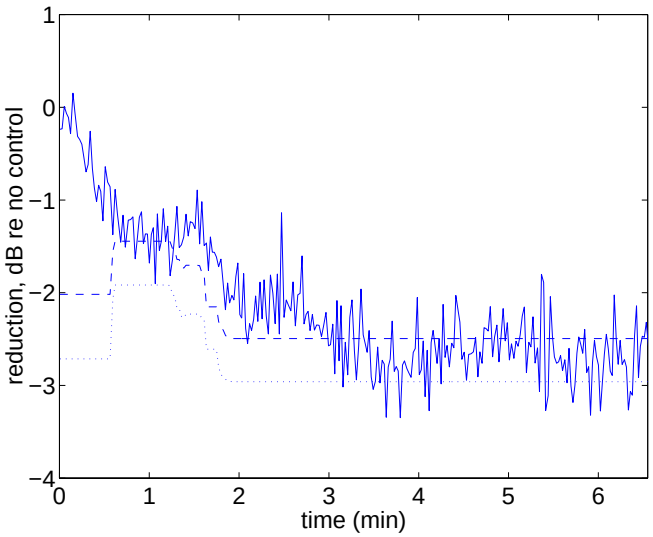

Figure 69. Reduction of 3rd Harmonic (Flight 2, run 6a): - measured; --predicted; ...predicted using unity coherence

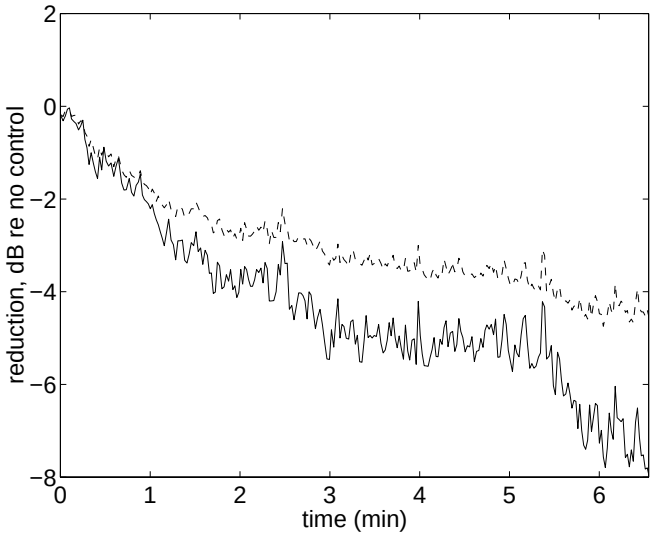

Figure 70. Reduction of Cost Function (Flight 2, run 3a): -linear; --A-weighted

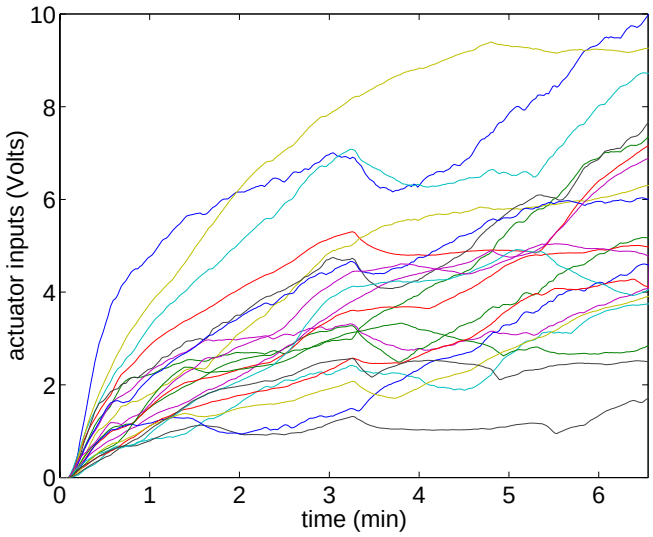

Figure 71. Actuator Input Voltages (Flight 2, run 3a)

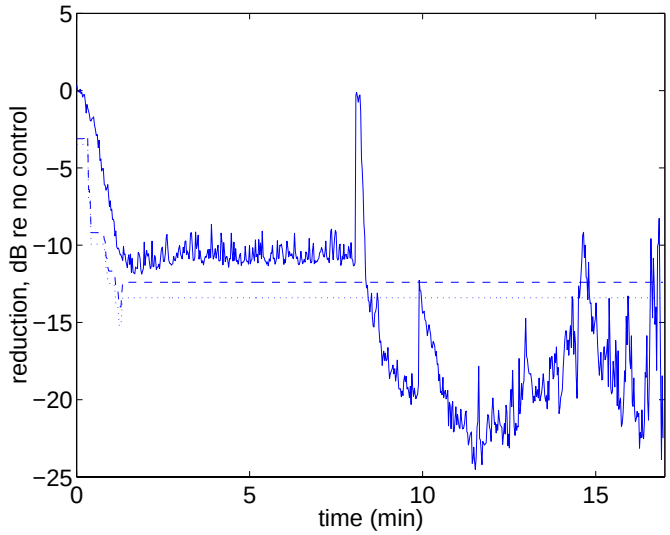

Figure 72. Reduction of 1st Harmonic (Flight 2, run 7a): -measured; --predicted; ...predicted using unity coherence

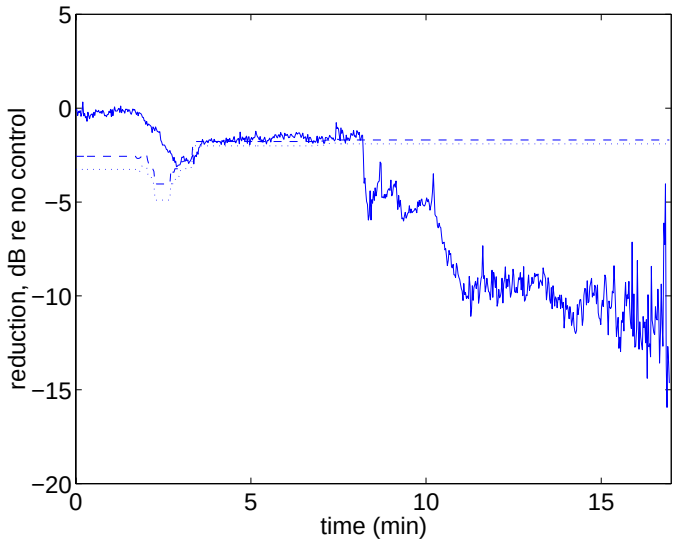

Figure 73. Reduction of 2nd Harmonic (Flight 2, run 7a): - measured; --predicted; ...predicted using unity coherence

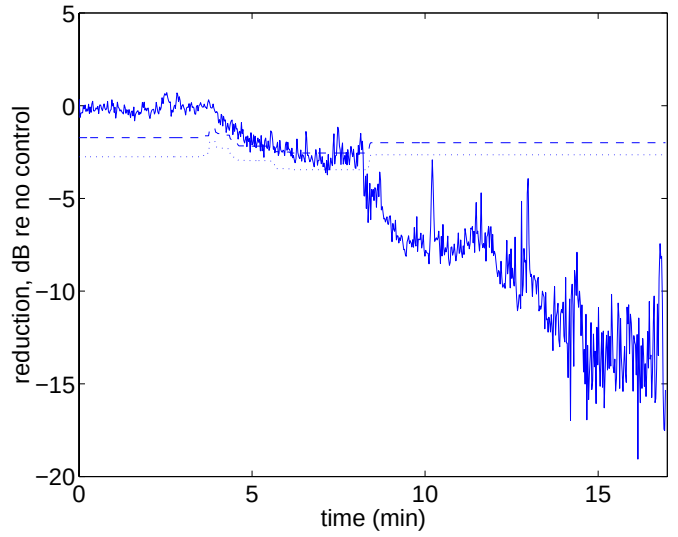

Figure 74. Reduction of 3rd Harmonic (Flight 2, run 7a): - measured; --predicted; ...predicted using unity coherence

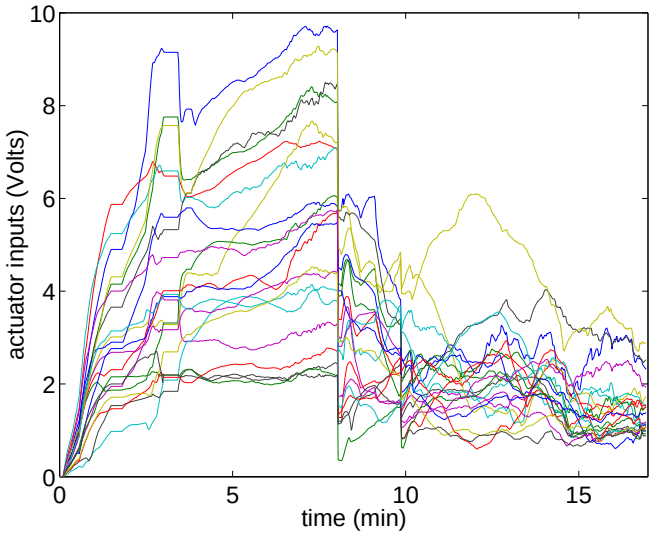

Figure 75. Actuator input voltages (Flight 2, run 7a)

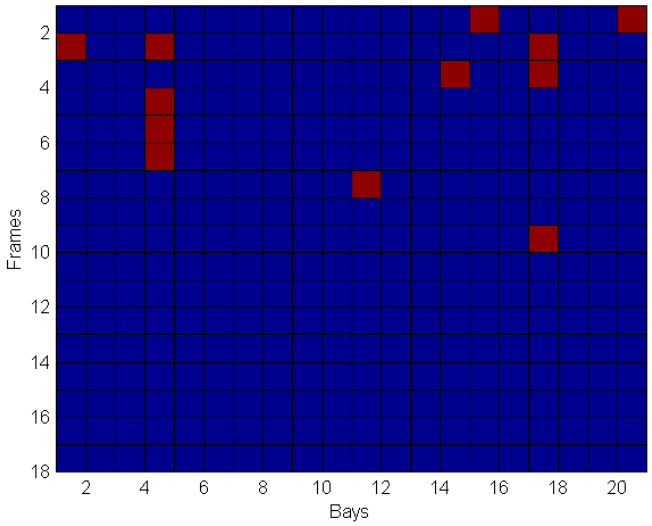

Figure 76. Location of 12 Actuators

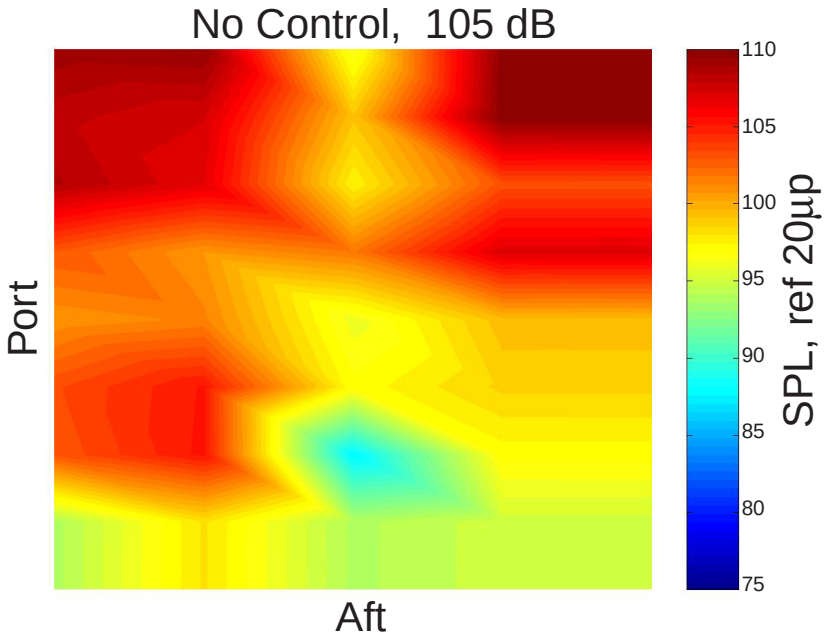

Figure 77 8 by 12 1st Harmonic, No Control

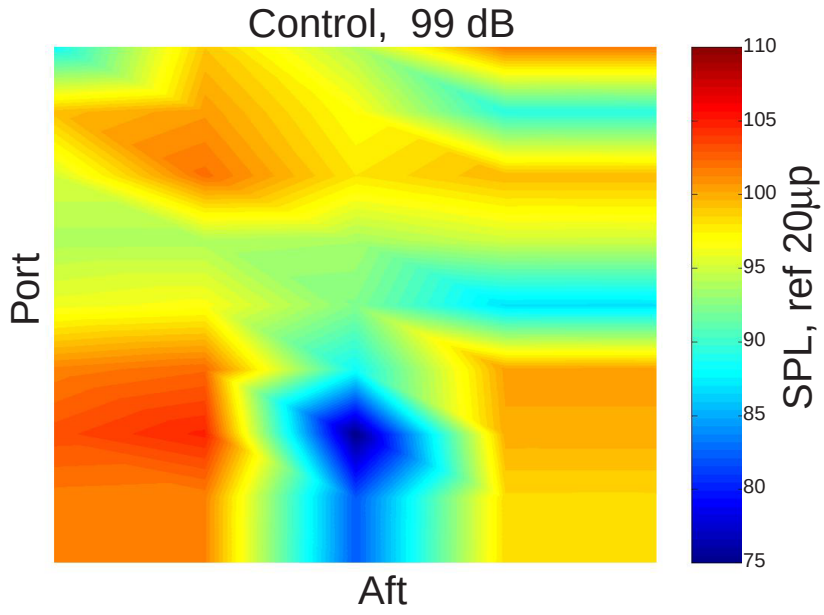

Figure 78. 8 by 12 1st Harmonic, Control

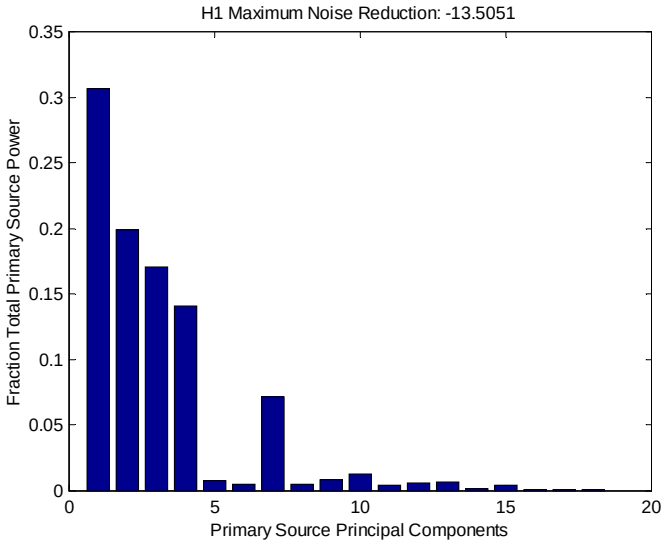

Figure 79. Principal Components of Primary Source Using Ground Transfer Functions

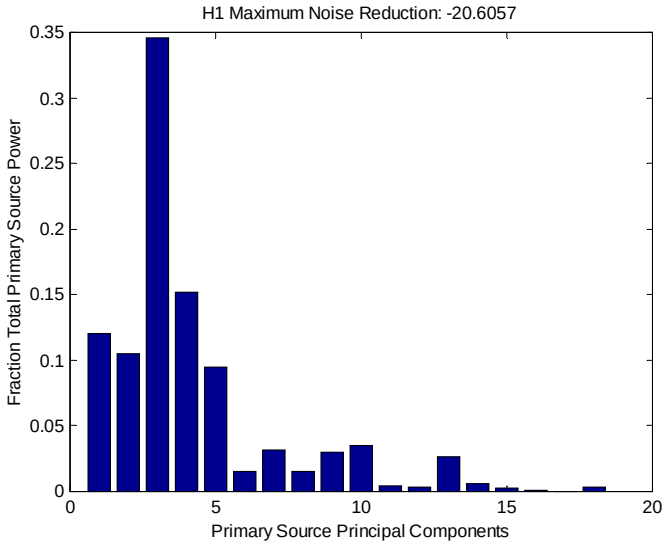

Figure 80. Principal Components of Primary source Using Flight Transfer Functions

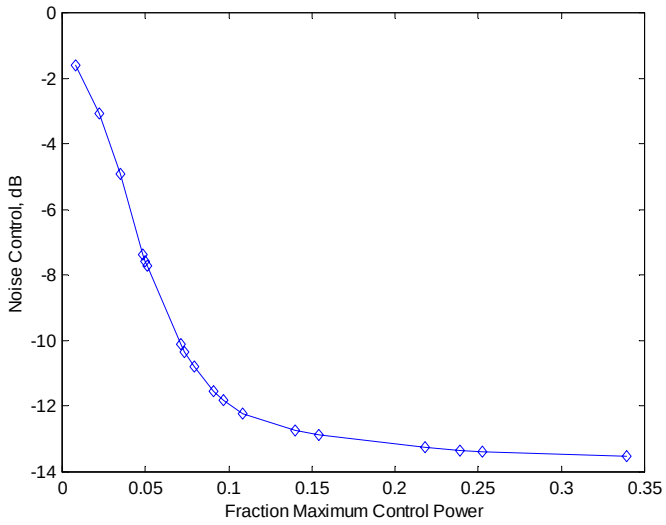

Figure 81. Potential Noise Control Using Ground transfer Functions

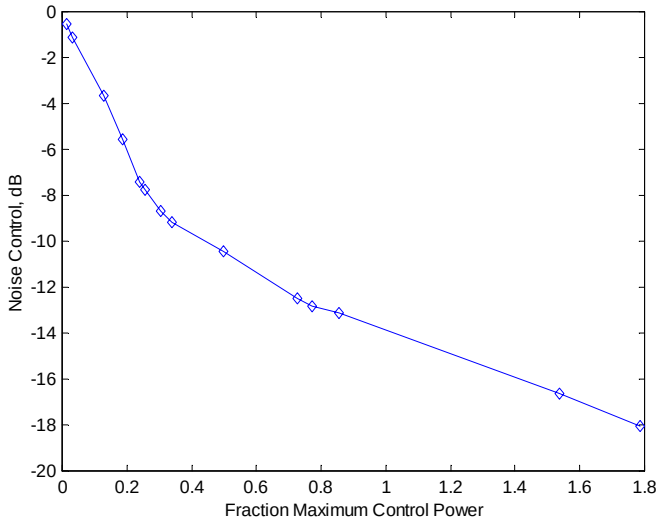

Figure 82. Potential Noise Control Using Flight Transfer Functions

REPORT DOCUMENTATION PAGE

Form Approved
OMB No. 0704-0188

1. AGENCY USE ONLY (*Leave blank*)	2. REPORT DATE	3. REPORT TYPE AND DATES COVERED
	March 2000	Technical Memorandom

4. TITLE AND SUBTITLE
Active Structural Acoustic Control of Interior Noise on a Raytheon 1900D

5. FUNDING NUMBERS
WU 538-03-14-01

6. AUTHOR(S)
Dan Palumbo, Ran Cabell, John Cline and Brenda Sullivan

7. PERFORMING ORGANIZATION NAME(S) AND ADDRESS(ES)
NASA Langley Research Center
Hampton, VA 23681-2199

U.S. Army Research Laboratory
Vehicle Technology Directorate
NASA Langley Research Center
Hampton, VA 23681-2199

8. PERFORMING ORGANIZATION REPORT NUMBER
L-17944

9. SPONSORING/MONITORING AGENCY NAME(S) AND ADDRESS(ES)
National Aeronautics and Space Administration
Washington, DC 20546-0001
and
U.S. Army Research Laboratory
Adelphi, MD 20783-1145

10. SPONSORING/MONITORING AGENCY REPORT NUMBER
NASA/TM-2000-209846
ARL-TR-2205

11. SUPPLEMENTARY NOTES
Palumbo, Cabell, Sullivan: Langley Research Center, Hampton, VA;
Cline: Vehicle Technology Directorate, ARL, Langley Research Center, Hampton, VA.

12a. DISTRIBUTION/AVAILABILITY STATEMENT
Unclassified-Unlimited
Subject Category 71 Distribution: Nonstandard
Availability: NASA CASI (301) 621-0390

12b. DISTRIBUTION CODE

13. ABSTRACT *(Maximum 200 words)*
An active structural acoustic control system has been demonstrated on a Raytheon Aircraft Company 1900D turboprop airliner. Both single frequency and multi-frequency control of the blade passage frequency and its harmonics was accomplished. The control algorithm was a variant of the popular filtered-x LMS implemented in the principal component domain. The control system consisted of 21 inertial actuators and 32 microphones. The actuators were mounted to the aircraft's ring frames. The microphones were distributed uniformly throughout the interior at head height, both seated and standing. Actuator locations were selected using a combinatorial search optimization algorithm. The control system achieved a 14 dB noise reduction of the blade passage frequency during single frequency tests. Multi-frequency control of the first 1st, 2nd and 3rd harmonics resulted in 10.2 dB, 3.3 dB and 1.6 dB noise reductions respectively. These results fall short of the predictions which were produced by the optimization algorithm (13.5 dB, 8.6 dB and 6.3 dB). The optimization was based on actuator transfer functions taken on the ground and it is postulated that cabin pressurization at flight altitude was a factor in this discrepancy.

14. SUBJECT TERMS
Active Noise Control, Active Structural Acoustic Control, Aircraft Interior Noise
Principal Component Control, Optimization

15. NUMBER OF PAGES
80

16. PRICE CODE
A05

17. SECURITY CLASSIFICATION OF REPORT	18. SECURITY CLASSIFICATION OF THIS PAGE	19. SECURITY CLASSIFICATION OF ABSTRACT	20. LIMITATION OF ABSTRACT
Unclassified	Unclassified	Unclassified	UL